

Characterising cosmic birefringence in the presence of galactic foregrounds and instrumental systematic effects

Baptiste Jost,¹ Josquin Errard,¹ and Radek Stompor^{2,1}

¹*Université de Paris Cité, CNRS, Astroparticule et Cosmologie, F-75013 Paris, France*

²*CNRS-UCB International Research Laboratory, Centre Pierre Binétruy, IRL2007, CPB-IN2P3, Berkeley, CA 94720, USA*

We study a possibility of constraining the isotropic cosmic birefringence with help of cosmic microwave background polarisation data without relying on any assumptions about the Galactic foreground angular power spectra and in particular on their EB correlation. We propose a new analysis framework aiming at measuring isotropic cosmic birefringence, based on a generalised parametric component separation approach, which accounts simultaneously on the presence of galactic foregrounds, relevant instrumental effects and external priors. We find that in the context of an upcoming multi-frequency CMB instrument, assuming in-lab calibration priors we are able to constrain instrumental polarisation angle for each frequency band and correct the observed sky component maps accordingly. We then produce an instrumental-effect-corrected and foreground-cleaned CMB map, which we use to estimate the isotropic birefringence angle and the tensor-to-scalar ratio, accounting on statistical and systematic uncertainties incurred during the entire procedure. In particular, in the case of a Simons Observatory-like, three Small Aperture Telescopes, we derive a uncertainty on the birefringence angle of $\sigma(\beta_b) = 0.07^\circ$, assuming calibration priors for all frequency channels with the precision of $\sigma_{\alpha_i} = 0.1^\circ$ and the standard cosmology. This implies that, using our method and given the calibration precision expected for current, the near future ground-based multi-frequency experiments could confirm or disprove the recently detected value of $\beta_b = 0.35^\circ$ with a significance of up to 5σ . We also find that, in the context of the current standard cosmological model, the impact of the polarisation angle miscalibration on the estimated value of the tensor-to-scalar ratio, r , and its precision, can be minimized using the methods proposed here and, as a result, to be subdominant as compared to uncertainties due to the foregrounds, the instrumental noise, and the CMB itself, independently on the assumed priors or lack thereof. Furthermore, we explore the impact on our results of precision of the calibration priors and of foreground complexity and obtain requirements on the calibration precision.

I. INTRODUCTION

Cosmic birefringence is an effect that rotates the polarisation angle of CMB photons. It can take many forms, depending on the details of the underlying physical mechanism. It can be isotropic or anisotropic, frequency dependent (similar to Faraday rotation), time dependent or constant. In this paper we focus on the case of time- and frequency- independent, isotropic birefringence. A rotation of the CMB polarisation angle needs a parity violating mechanism. This can be due to multiple reasons ranging from a violation of the Lorentz symmetry [1] to the impact of specific dark-energy models [2] or dark-matter axion-like particles through the Chern-Simons effect [3, 4]. This parity violation will lead to non-zero EB correlation, even if the primordial EB correlation is zero as for instance in the standard cosmology. Hereafter we will denote the isotropic birefringence angle as β_b and assume no primordial EB correlation, i.e., $C_\ell^{EB} = 0$. The proposed framework is however adaptable to any non-zero primordial EB correlations, as predicted by e.g. anisotropic inflation models [5] or an asymmetry in primordial GW handedness [6, 7] (chiral gravitational waves).

Detecting cosmic birefringence is of significant scientific importance on its own, as is understanding consequences of its presence as well as of the presence of po-

larisation angle miscalibration on the estimation of other cosmological parameters such as the tensor-to-scalar ratio, r [8]. For instance, it has been argued that in the case of the Simons Observatory (SO) reaching the precision goal on r of $\sigma(r) \approx 10^{-3}$ [9] requires the precision on the polarisation angle of a few tenths of a degree [8]. For LiteBIRD [10], aiming at constraining $r \leq 10^{-3}$, the polarisation angle precision requirements are even more stringent ranging between an arcminute and a few tens of arcminutes depending on the frequency channel [11]. The goal of this work is to address both these problems within a single, self-contained framework, we develop here for this purpose.

The detection of an isotropic cosmic birefringence is difficult due to a degeneracy of the birefringence angle with the absolute calibration of the polarisation angle of the CMB telescope, denoted α . It is further confounded by the galactic foregrounds, properties of which are not yet well understood, and which have to be accounted on in the presence of instrumental effects.

In some specific cases such as the case of a time dependent birefringence, the degeneracy can be broken if the polarisation angle of the telescope can be assumed stable, even if potentially unknown, in time therefore allowing for disentangling the two effects. As recently demonstrated by BICEP [12, 13] and SPT [14] teams such approaches can indeed be used successfully to constrain time dependent birefringence and thus to set con-

straints on axion oscillations and, as a result, the axion-photon coupling in the axion mass range given by the oscillation frequency range accessible by the analysis.

In the case of a time-independent and isotropic birefringence no such resorts are possible and one has to deal explicitly with its degeneracy with the polarisation angles of the telescopes.

One popular approach is called the self-calibration method [15]. This method fixes the polarization angle so that the EB correlations of the signal contained in a map vanishes. However, although it is effective in attaining the precision required for r , by assumption it rules out any possible detection of isotropic cosmic birefringence. Moreover, the self-calibration requires that the EB cross-correlation vanishes for all the signals contained in a considered map, be they CMB or foregrounds. Consequently, to not rely on any assumptions about the properties of the foregrounds, the method should be applied to the foreground-cleaned CMB maps as produced at the outcome of the component separation procedures. For multifrequency observations with potentially different miscalibration angles at different frequencies. This however requires understanding of the impact of such effects on the component separation as studied in detail in the following.

Minami *et al.* proposed in [16] another method to lift the degeneracy between polarisation angle and birefringence, further elaborated on in Diego-Palazuelos *et al.* [17]. It relies on an assumed model for the EB power spectrum of the foregrounds. With such a model we can then estimate the polarisation angle of the telescope by fitting the parameters of the foreground EB with observations. The first results using this method are very promising and potentially hinting at non-zero isotropic birefringence with $\beta_b = 0.35^\circ \pm 0.14^\circ$ [18] using Planck data sets. Diego-Palazuelos *et al.* [17] found similar results but had to assume more complex foreground models such as filament models from Clark *et al.* [19] and Hufferberger *et al.* [20] as well as the COMMANDER sky model [21] to ensure that the found value of birefringence angle is independent on the area of observed sky. Even more recently Eskilt and Komatsu [22] used this method with the previously mentioned EB models on Planck and WMAP data and found $\beta_b = 0.37^\circ \pm 0.14^\circ$ with $f_{sky} = 0.62$ and $\beta_b = 0.342^\circ \pm_{-0.091^\circ}^{+0.094^\circ}$ with $f_{sky} = 0.92$. They also found results consistent with a frequency independent birefringence angle such as in the Planck PR4 only case [23].

These are very promising results, potentially hinting at the non-zero birefringence. However, the common assumption behind these results concerns the EB angular power spectrum of the foregrounds for which lack reliable models or measurements at this time.

In this work we study a complementary option invoking a use of calibrations of the polarisation angle of the telescopes. We first generalise a parametric component separation method as applied to multi-frequency Stokes maps so it can correct jointly for instrumental effects and cleaning complex foregrounds, while capitalising on the

presence of appropriate priors. We then assess the impact of this procedure on the joint estimation of the birefringence angle, β_b , and the tensor to scalar ratio, r . The proposed approach can be seen as a practically viable implementation of the self-calibration approach of [15], amended to allow for the estimation of the birefringence angle, and explicitly dealing with the foreground contaminations.

We also turn this approach into a forecasting tool in order to derive realistic and robust, ensemble-averaged constraints on the cosmological parameters, β_b and r , but also to provide precision requirements for the calibration priors.

For completeness we note that other promising methods have been proposed, which are pertinent to a detection of the birefringence effects. This includes the birefringence tomography of [24] aiming at measuring the difference between a birefringence angle induced at recombination and one at reionisation (respectively small and large angular scales of the CMB spectra) and therefore at constraining the change of the birefringence angle between the two corresponding redshifts.

II. BACKGROUND

A. Cosmic Birefringence

The effect of the birefringence on the primordial CMB power spectra C_ℓ^{XY} can be written as follows:

$$\begin{aligned}\tilde{C}_\ell^{EE} &= C_\ell^{EE} \cos^2(2\beta_b) + C_\ell^{BB} \sin^2(2\beta_b) \\ \tilde{C}_\ell^{BB} &= C_\ell^{EE} \sin^2(2\beta_b) + C_\ell^{BB} \cos^2(2\beta_b) \\ \tilde{C}_\ell^{EB} &= (C_\ell^{EE} - C_\ell^{BB}) \frac{\sin(4\beta_b)}{2},\end{aligned}\tag{1}$$

where we use a tilde \tilde{C}_ℓ^{XY} to denote the spectra as measured in the presence of the birefringence. The spectra unaffected by birefringence, C_ℓ^{XY} , can be assumed to include the lensing effect, as isotropic birefringence commutes with lensing as it is scale independent. This is due to the fact that the lensing effect does not depend on the coordinate frame while the effect of isotropic birefringence can be seen as merely a coordinate change. The effect of a non-zero birefringence angle on the CMB power spectra is depicted in Fig 1.

B. Polarisation-Angle Calibrators

Many calibration methods are available for the polarisation angle of the telescope. One of the standards for calibration is to use astrophysical objects, such as the measurements of the polarisation angle of Tau A (Crab Nebula) for which the polarisation angle is measured as $-88.19^\circ \pm 0.33^\circ$ by Aumont *et al.* [25], and its frequency dependence seems to be well modelled by a single power

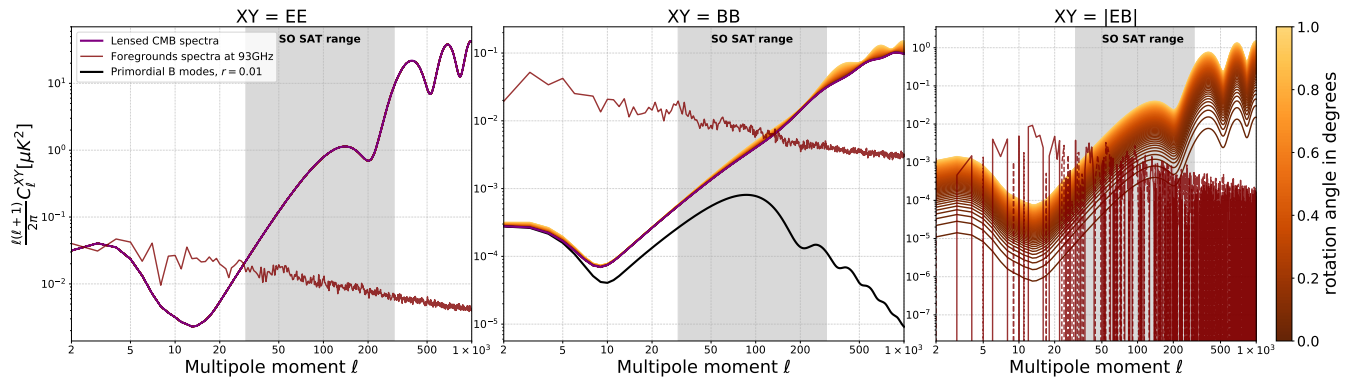


FIG. 1. Impact of an isotropic birefringence angle on the CMB lensed spectra. The galactic foregrounds power spectra, unaffected by birefringence and estimated here at 93GHz on a $f_{\text{sky}} \approx 10\%$ SO SAT-like patch [9], are represented in dark-red.

law spectrum as shown by Ritacco *et al.* [26]. These measurements are reaching high precision of interest for forthcoming CMB efforts, however they rely on astrophysical modelling of the signal and discrepancies both in the polarisation angle values and its precision appear between frequencies probably due to the difference between instruments and their systematics.

Another approach capitalises on human-made calibrators. Albeit challenging, great improvements have been made recently and new techniques have been tested on current as well as future ground-based CMB experiments. For instance a mobile rotating wire grid placed on top of a telescope's optic chain could act as a polarising filter. By comparing the position of the filter and the signal received by the detectors one can estimate the polarisation angle of the latter. For example the Simons Observatory (SO) plans on deploying such devices on their Small Aperture Telescopes (SATs) and the current goal is to estimate the polarisation angles with a precision below 1° [27].

One other method consists in a drone carrying a polarised source calibrated in the lab and which would hover above a telescope so that it would be in its far field. By knowing the relative position of the drone with respect to sky coordinates using either a star camera or a camera pointing at the ground, one can then estimate the polarisation angle of the telescopes. The current forecast for this method is $0.01^\circ \leq \sigma(\alpha) \leq 0.1^\circ$, and can be achieved in several frequency channels [28]. This technique is being tested on several telescopes in the Atacama such as ACT [29, 30] and CLASS [31] and is also planned to be applied to SO SATs.

C. Galactic Foregrounds and Component Separation

These progresses are very encouraging and it seems therefore reasonable to expect that forthcoming CMB experiments will have the polarisation angles determined

with a high precision for at least some of the frequency channels, therefore providing information necessary for a robust measurement of the isotropic birefringence. However, the impact of the precision of the calibrators on such an measurement also depends on the presence in the data of non-cosmological signals, such as galactic foregrounds. The eventual CMB map will have to be first cleaned of such effects as part of a procedure referred to as component separation. It is therefore important to understand the interplay between the polarisation angle uncertainties and the component separation step and to account on their impact in order to produce high fidelity, reliable results. Similarly, these effects should also be taking into account in reliable performance forecasting to lead to reliable polarisation angle requirements for the calibration campaigns.

Galactic foregrounds have been identified as one of the major contaminant for the detection of primordial B modes and numerous efforts have been made on their characterisation, modelling, and on the development of new foreground cleaning algorithms. These range from semi-blind methods, such as, ILC [32], GNILC [33], Needlet ILC [34] to cite a few, to parametric approaches, such as SMICA [35] and COMMANDER [36, 37] for instance, which have been implemented in the pixel, harmonic, and wavelets domains.

In this work, we employ pixel-domain parametric component separation methods as described in Stompor *et al.* [38] and generalised in Vergès *et al.* [39] to include instrumental parameters. The pixel-domain methods assume inputs in a form of single frequency maps with well characterised uncertainties. The standard parametric methods assume frequency scaling laws for all the galactic foregrounds, which can be parameterised with a handful of parameters. The parameters are subsequently estimated during the component separation process and used to separate the single frequency maps into maps of sky components. The separated maps of the CMB signal can be then further used to derive constraints on cosmological parameters in a follow-up step referred to as a

cosmological parameter estimation.

In the generalised parametric component separation, in addition to the parameters characterising the foreground scaling laws we introduce parameters describing instrumental effects and estimate all of them together. We then use both sets of the parameters to derive maps of sky components. This allows not only for deriving better data models, driven by the information about the instrumental parameters contained in the data themselves, but also incorporates the impact of the instrumental parameter estimation on that of the foreground parameters.

The entire process from the single frequency maps up to the cosmological parameters, and thus consisting of the parametric component separation followed by the cosmological parameter estimation, can be performed in separate steps as in [38]. Alternately, it can be implemented as a single step, e.g., in Eriksen *et al.* [37]. While this latter approach allows for statistically robust propagation of the statistical uncertainties throughout out the entire process the former are often simpler from the implementation point of view and computationally more efficient. They however need to face a problem of characterising the uncertainties of the derived component maps.

In either approach a fundamental problem is how to assess the effects of a mismatch between the assumed foreground scaling laws or the actual frequency dependence of the sky components. This issue is usually addressed by investigating the performance of the method within a family of plausible actual sky models. In this context, [40] has proposed an efficient, semi-analytic approach allowing for evaluating the impact of the foreground properties mismatch on the cosmological parameter estimation. While the formalism proposed there provides a blue print for an analysis of actual data, it has been shown to be particularly useful in forecasting the performance of future and currently designed experiments permitting a quick evaluation of multiple experimental configurations, [39, 41–43].

In this work we extend the original formalism and propose a novel generalised parametric component separation that allows to account for the frequency-channel dependent, polarisation angle misalignment simultaneously with foreground cleaning capitalising on assumed calibration priors. Similarly as for Minami and Komatsu [18] we suppose that birefringence only acts on the CMB signal and not on foregrounds. As in the earlier work the formalism can be easily adapted for an actual data analysis, however we specialise it here for performance forecasting. Consequently, we use the formalism to characterise the effect of this generalised component separation method and therefore include the effects due to polarisation angle miscalibration on the estimation of cosmological parameters and forecast its performance in the particular case of SO. Conversely, we also discuss precision requirements for the polarisation angle calibration given the targeted precision of the estimation of the isotropic birefringence angle, β_b .

III. METHOD

Our method is composed of two steps. The first step consists in the simultaneous estimation of foreground and instrumental parameters performed as part of the generalised parametric component separation described in Stompor *et al.* [40]. It is based on a generalised version of the so called spectral likelihood, which yields constraints on foreground and instrumental parameters. These are then used to derive estimates of the sky components including that of the CMB, as well, as their generalised statistical uncertainties.

Parametric component separation assumes some parametric frequency scaling for all the relevant components. These scalings may not provide an adequate description of the actual sky components therefore leading to both statistical uncertainties and biases on the scaling parameters. Consequently, the resulting map uncertainties include contributions due to the instrumental noise as contained in the input single frequency maps and foreground residuals resulting from statistical uncertainties on the estimated spectral parameters. We refer to these hereafter as statistical residuals. These are to be distinguished from systematic residuals, e.g., due to a mismatch between the assumed and actual frequency scaling for some of the components, which, while potentially present in the estimated component maps, are a priori unknown and therefore remain unaccounted for in the maps statistical description. The foreground models used to generate mock data sets and those assumed in their analysis, are detailed in subsection IV C.

Both instrumental and foreground parameters are thus unknowns of a global fitting problem, however, the manner in which they impact the entire procedure is rather different. The foreground parameters are sky-component specific and depend on the assumed model, hence they do not depend on the number of available frequency channels. More channels permits in general better estimation of the foreground parameters. This is not always so for the instrumental parameters, as they are commonly specific to frequency channels and more frequencies typically mean more parameters. This is for instance the case of the polarisation angle misalignment as discussed in detail later in this work. (See Vergès *et al.* [39] for a counter example). In such cases increasing the number of available channels may not improve the problem stability and instead other means, such as priors, may need to be incorporated in the component separation formalism.

The second step then constrains cosmological parameters from the CMB maps and their covariances as derived on the first step. This is done with help of the likelihood obtained assuming that CMB signal is (nearly) Gaussian and isotropic and its covariance is given by the CMB power spectra, which in turn depend on cosmological parameters. Consequently, the covariance model does not account on the presence of residuals in the CMB map as estimated on the first step. This may then lead to systematic errors in the estimated parameters.

Symbol	Definition
$\hat{\cdot}$	Denotes true parameter, signal or operator
\mathbf{A}	Effective mixing matrix
s	Effective sky signal
\mathbf{W}	Map operators
Γ	Set of spectral and instrumental parameters

TABLE I. Notation conventions.

The proposed method could be applied directly to actual or simulated data, however, our main goal here is to provide robust performance forecasts and provide calibration requirements for future CMB experiments. We could do so by relying on a massive Monte Carlo approach, applying the procedure to simulated data sets. Alternately, instead of dealing directly with the likelihoods and input, single frequency maps, we derive and use likelihoods averaged of statistical ensemble of the CMB and noise realisations and instead of single frequency maps we use respective data covariance matrices. These have to account on the CMB signal and noise but also on the residuals present in the estimated CMB map. Their calculation requires therefore actual (noise-free) component maps for each considered component as included in the simulations. While this approach requires occasionally some additional simplifications, they do not affect the quality of our projections, while the resulting method is computationally efficient allowing to investigate a large number of models and putative experiments. Our forecasting pipeline is shown in Fig. 2.

We describe the entire procedure in detail below, starting from the data model we assume, then the first step involving the generalised spectral likelihood and finally the second step involving the cosmological likelihood and sampling.

A. Data Model

The input for the component separation step are single frequency maps reconstructed from actual measurements of a CMB experiment. These maps are gathered in a single data vector \mathbf{d} ; for each sky pixel we store the measured sky amplitudes for each frequency, so \mathbf{d} contains $n_{\text{stokes}} n_f$ maps. To retrieve the different components that make up the measured signal we model it as:

$$\mathbf{d} = \mathbf{X} \mathbf{A} \mathbf{B} \mathbf{c} + \mathbf{n} \quad (2)$$

with \mathbf{n} standing for the noise in each map; \mathbf{c} is a vector containing all maps of the sky signals concatenated together. It contains therefore $n_{\text{stokes}} \times n_{\text{comp}}$ maps. \mathbf{B} acts on \mathbf{c} and models the impact of birefringence on the *lensed* CMB. \mathbf{A} is the mixing matrix that acts on the component vector synthesising them into the corresponding frequency maps for each observation channel of the considered telescope.

Finally \mathbf{X} is the instrumental response matrix that models how the instrument's characteristics may affect

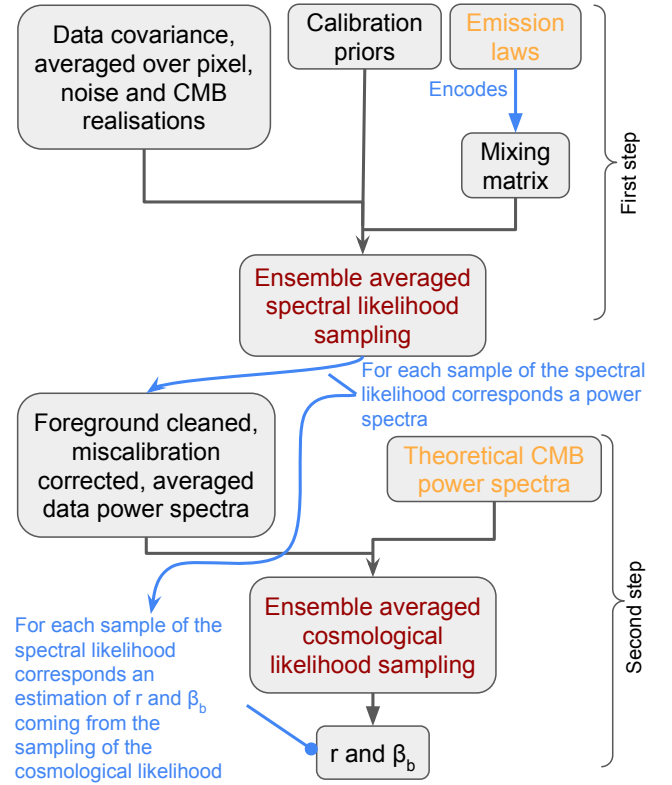


FIG. 2. Diagram describing the different steps of the method in its forecasting rendition. In red are the two steps of the algorithm, in orange are the main assumptions going in to built the likelihood, and in black the various input and outputs of the two steps.

the sky signal at each frequency.

The data covariances which are needed as input for our forecasting method, Fig. 2, are then computed averaging over statistical ensemble of product of the data vector, \mathbf{d} , expressed as above.

We define the mixing matrix for each sky pixel p as $\mathbf{A}_p(\{\beta_{fg}\})$, which scales the sky component amplitudes in frequency and co-adds them together. Each column of \mathbf{A} corresponds to a component and each row to an observation frequency and each considered Stokes parameter, either Q or U in the following. The scaling of foreground components with respect to frequency is assumed to be parameterised by a set of spectral parameters $\{\beta_{fg}\}$. We place ourselves in CMB units so that the elements of \mathbf{A} acting on the CMB sky signal are all equal to 1. The mixing matrix has $(n_{\text{stokes}} \times n_f) \times (n_{\text{stokes}} \times n_{\text{comp}})$ elements. Here the mixing matrix does not mix between different Stokes parameters and corresponding elements of the mixing matrix vanish, leaving only $n_{\text{stokes}} \times n_f \times n_{\text{comp}}$ non-zero elements, and the elements of \mathbf{A} corresponding to Q & U are equal.

Hereafter, we focus on isotropic cosmic birefringence \mathbf{B} and consider polarisation angle misalignment as the only instrumental effects. We therefore consider only Q and U Stokes parameter maps, both on the input and the out-

put of the component separation procedure. Therefore, from now on $n_{\text{stokes}} = 2$. The formalism, which follows, can be straightforwardly generalised to include any combination of the Stokes parameters, if needed. The general rotation matrix in Q & U space for the spin 2 polarisation vector is denoted $\mathcal{R}(\alpha)$ and is defined as¹:

$$\begin{pmatrix} Q_{out} \\ U_{out} \end{pmatrix} = \begin{pmatrix} \cos(2\alpha) & \sin(2\alpha) \\ -\sin(2\alpha) & \cos(2\alpha) \end{pmatrix} \begin{pmatrix} Q_{in} \\ U_{in} \end{pmatrix} \quad (3)$$

$$\equiv \mathcal{R}(\alpha) \begin{pmatrix} Q_{in} \\ U_{in} \end{pmatrix}.$$

Effects of cosmic birefringence on the map level can be represented as a block diagonal matrix, with each block corresponding to a different component. Birefringence acts on the CMB Q & U elements of \mathbf{c}_p with a rotation matrix $\mathcal{R}(\beta_b)$, and with β_b the birefringence angle. The other blocks of \mathcal{B} are 2×2 identity matrices since we assume here that birefringence does not affect components other than CMB. For definiteness, we will assume that properties of the 'primordial' CMB, i.e., as contained in the component vector, \mathbf{c} , are well-defined and known, and for simplicity throughout this paper, we will take the 'primordial' CMB EB cross-correlation to be zero. This makes the definition of the birefringence angle (in the absence of other effects studied below) well defined. However, incorporating the cases with some specific, non-vanishing, 'primordial' EB correlations is straightforward. We also note that the framework could be generalised to the anisotropic case by simply allowing the birefringence angle to vary between sky pixels.

\mathbf{X} is the instrumental response matrix, it can be applied to many instrumental effects such as but not limited to half-wave plate systematic, band-passes, polarisation efficiency, polarisation angle miscalibration etc. Miscalibration of the polarisation angle is particularly relevant for the search of birefringence angle. We chose to model polarisation miscalibration with one angle by frequency channel for simplicity. One could modify the *coarseness* of the model to adjust for specific experiment conditions. Refining it with one angle per focal plane wafer or on the contrary use one angle per multi-frequency instrument for instance. With this assumption we can model the miscalibration of polarisation angles as a rotation matrix acting on pixels of Q & U maps of a particular frequency channel. Therefore we construct $\mathbf{X}(\{\alpha_1, \dots, \alpha_{n_f}\})$ as a block diagonal matrix, each block is a rotation matrix $\mathcal{R}(\alpha_i)$ acting on the Q & U components of the i^{th} frequency channel of the vector given by $\mathbf{A}_p(\{\beta_{fg}\}) \mathcal{B}(\beta_b) \mathbf{c}_p$.

Here it is interesting to notice that the birefringence modifies the mixing matrix *column* wise and of course only for the column corresponding to the CMB signal. This can

be seen as a re-definition of the amplitude of the CMB. While this effect could be dealt with in pixel space it is not straightforward and we will treat it in power spectra. In particular the prior that we use on primordial CMB signal having no EB correlation would also need to be transformed for the estimation of β_b which would be cumbersome. This is why we redefine the sky signal to an effective sky signal after birefringence as: $\mathbf{s}_p \equiv \mathcal{B}(\beta_b) \mathbf{c}_p$. The miscalibration angles however can, and should, be handled at the same time as foreground spectral indices. So in the following we denote the effective mixing matrix as $\mathbf{A}_p(\{\Gamma\}) \equiv \mathbf{X}(\{\alpha_1, \dots, \alpha_{n_f}\}) \mathbf{A}_p(\{\beta_{fg}\})$. We call the set of parameters used to characterise \mathbf{A}_p : $\{\Gamma\} \equiv \{\{\alpha\}, \{\beta_{fg}\}\}$ where $\{\alpha\} \equiv \{\alpha_1, \dots, \alpha_{n_f}\}$, generic elements of $\{\Gamma\}$ will be referred to as γ . From this data model we can perform a generalised parametric component separation with both the cleaning of astrophysical foregrounds and the correction of instrumental systematic effects using the spectral likelihood formalism developed in Stompor *et al.* [38]. Finally the data vector for each sky pixel \mathbf{d}_p is defined in Eq. 4 below:

$$\mathbf{d}_p = \underbrace{\mathbf{X}_p(\{\alpha_1, \dots, \alpha_{n_f}\}) \mathbf{A}_p(\{\beta_{fg}\})}_{\mathbf{A}_p} \underbrace{\mathcal{B}(\beta_b) \mathbf{c}_p}_{\mathbf{s}_p} + \mathbf{n}_p \quad (4)$$

Let us consider an arbitrary instrumental angle α_0 , we can always write,

$$\begin{aligned} \mathbf{X}_p(\{\alpha_1, \dots, \alpha_{n_f}\}) &= \mathbf{X}(\{\alpha_1 - \alpha_0, \dots, \alpha_{n_f} - \alpha_0\}) \\ &\times \mathbf{X}_p(\{\alpha_0, \dots, \alpha_0\}) \\ &= \mathbf{X}_p(\{\alpha'_1, \dots, \alpha'_{n_f}\}) \mathbf{X}_p(\{\alpha_0, \dots, \alpha_0\}), \end{aligned} \quad (5)$$

where all the angles with a prime include an extra common rotation by an angle $-\alpha_0$ and the rightmost factor in the last equation rotates all channels by the same angle α_0 to compensate for this. We note that rotating all frequency channels by the same angle is equivalent to rotating all sky components by the very same angle, i.e.,

$$\mathbf{X}_p(\{\alpha_0, \dots, \alpha_0\}) \mathbf{A}_p \mathbf{s}_p = \mathbf{A}_p \tilde{\mathbf{X}}_p(\{\alpha_0, \dots, \alpha_0\}) \mathbf{s}_p, \quad (6)$$

where $\tilde{\mathbf{X}}_p$ is a rotation operator analogous to \mathbf{X}_p but operating on sky components instead of frequency channels and for definiteness we assume, as always, that CMB is the first component. We can therefore rewrite the signal term of our data model in Eq. 4 as,

$$\begin{aligned} \mathbf{A}_p \tilde{\mathbf{X}}_p(\{\alpha_0, \dots, \alpha_0\}) \mathcal{B}(\beta_b) \mathbf{c}_p &= \\ &= \mathbf{A}_p \tilde{\mathbf{X}}_p(\{\alpha_0 + \beta_b, \dots, \alpha_0\}) \mathbf{c}_p \\ &= \mathbf{A}_p \mathcal{B}(\alpha_0 + \beta_b) \mathbf{c}'_p, \end{aligned} \quad (7)$$

where the new sky components, \mathbf{c}' , contain the same CMB signal as \mathbf{c} , but the foregrounds are modified due to the rotation by the angle α_0 . In the absence of any additional assumptions both \mathbf{c} and \mathbf{c}' and the corresponding birefringence angles, β_b and $\beta_b + \alpha_0$, provide legitimate solution to the problem consistent with the data, \mathbf{d} . Consequently, the problem does not have a unique solution

¹ Note that some references use the other sign convention for the rotation matrix, however this does not affect the results presented in this work.

for foreground components and the birefringence angle. In practice this implies that employing any of the standard methods of solving the inverse problem in Eq. 4 is going to have a degeneracy and that we will need some additional assumptions to break it. These extra assumptions could concern any of the foreground components, e.g., by defining their EB cross-correlations, as done, for instance, in the approaches of [16, 17], or provide some external constraints on the common rotation angle, α_0 . While both of these could be considered in the framework proposed here, this is the second option we focus on in the following.

B. Joint Parametric Component Separation and Systematic Effects Correction

1. Parameter Estimation

We adapt the fiducial parametric component separation methods of Stompor *et al.* [40] to take into account the generalised data model, Eq. 4. Replacing the standard mixing matrix of [40] with the effective mixing matrix $\mathbf{\Lambda}_p$ and the sky signal vector with the effective one s_p allows us to jointly fit for systematic effects and foreground parameters. Depending on the considered systematic effects some parameters might be degenerate, such as the absolute polarisation angles of the detectors. Some of these degeneracies can be lifted using calibration priors. But the impact of those on the statistical error of the parameter estimation needs to be assessed and propagated correctly throughout the pipeline.

Similarly to Vergès *et al.* [39], adapting the spectral likelihood marginalised over sky signals from [40] results in the following log-likelihood:

$$\begin{aligned} S &\equiv -2 \ln(\mathcal{L}(\{\Gamma\})) \\ &= \text{cst} - \sum_p \text{tr} \left(\mathbf{N}_p^{-1} \mathbf{\Lambda}_p (\mathbf{\Lambda}_p^t \mathbf{N}_p^{-1} \mathbf{\Lambda}_p)^{-1} \mathbf{\Lambda}_p^t \mathbf{N}_p^{-1} \mathbf{d}_p \mathbf{d}_p^t \right) \end{aligned} \quad (8)$$

where \mathbf{N}_p is the noise covariance matrix. Optimising this likelihood gives us an estimation of both foregrounds parameters β_{fg} and instrumental parameters $\{\alpha\}$. This is the likelihood we would use while analysing a specific, actual or simulated, data set. In the forecasting proce-

dure we average the likelihood over both CMB and noise realisation similarly as in [40] :

$$\langle S \rangle = - \sum_p \text{tr} \left((\mathbf{N}_p^{-1} - \mathbf{P}_p(\{\Gamma\})) \langle \mathbf{d}_p \mathbf{d}_p^t \rangle \right) \quad (9)$$

where \mathbf{P}_p is the projection operator defined as:

$$\mathbf{P}_p(\{\Gamma\}) \equiv \mathbf{N}_p^{-1} - \mathbf{N}_p^{-1} \mathbf{\Lambda}_p (\mathbf{\Lambda}_p^t \mathbf{N}_p^{-1} \mathbf{\Lambda}_p)^{-1} \mathbf{\Lambda}_p^t \mathbf{N}_p^{-1} \quad (10)$$

and $\langle \mathbf{d}_p \mathbf{d}_p^t \rangle$ is given by:

$$\begin{aligned} \langle \mathbf{d}_p \mathbf{d}_p^t \rangle &= \langle \hat{\mathbf{\Lambda}}_p \hat{s}_p \hat{s}_p^t \hat{\mathbf{\Lambda}}_p^t \rangle + \langle \mathbf{n}_p \mathbf{n}_p^t \rangle \\ &= \mathbf{\Lambda}_p(\{\hat{\Gamma}\}) \langle \hat{s}_p \hat{s}_p^t \rangle \mathbf{\Lambda}_p^t(\{\hat{\Gamma}\}) + \mathbf{N}_p \end{aligned} \quad (11)$$

In Eq. 11, $\hat{\mathbf{\Lambda}}_p$ is $\mathbf{\Lambda}_p$ evaluated at the true values of parameters $\{\hat{\Gamma}\}$ for both instrumental parameters $\{\hat{\alpha}\}$ and foreground parameters $\{\hat{\beta}_{fg}\}$.

\hat{s}_p is the true effective sky signal containing CMB and foregrounds.

One can express $\hat{\mathbf{\Lambda}}_p$ and \hat{s}_p in such a way as to distinguish between the CMB terms and the foregrounds term in Eq. 11. \hat{s}_p^{cmb} represents the two rows of \hat{s}_p that correspond to the Q & U CMB signals, and \hat{s}_p^{fg} the leftover components. Similarly $\hat{\mathbf{\Lambda}}_p^{\text{cmb}}$ is made of the two columns of $\hat{\mathbf{\Lambda}}_p$ that act on the CMB components in \hat{s}_p , and $\hat{\mathbf{\Lambda}}_p^{\text{fg}}$ the other columns. Eq. 11 becomes:

$$\begin{aligned} \langle \mathbf{d}_p \mathbf{d}_p^t \rangle &= \hat{\mathbf{\Lambda}}_p^{\text{cmb}} \langle \hat{s}_p^{\text{cmb}} \hat{s}_p^{\text{cmb},t} \rangle \hat{\mathbf{\Lambda}}_p^{\text{cmb},t} \\ &\quad + \hat{\mathbf{\Lambda}}_p^{\text{fg}} \hat{s}_p^{\text{fg}} \hat{s}_p^{\text{fg},t} \hat{\mathbf{\Lambda}}_p^{\text{fg},t} + \mathbf{N}_p \end{aligned} \quad (12)$$

In the case of a non-parametrisable model one could replace $\hat{\mathbf{\Lambda}}_p^{\text{fg}} \hat{s}_p^{\text{fg}}$ by the frequency maps of the considered foregrounds after the action of the miscalibration matrix. The *parametric* model used in the effective mixing matrix $\mathbf{\Lambda}_p$ would then mismatch with the data and could lead to foreground residuals and a bias in the cosmological parameters. The average over CMB and noise realisations does not affect \hat{s}_p^{fg} and we use the output frequency maps from PySM to compute the $\hat{s}_p^{\text{fg}} \hat{s}_p^{\text{fg},t}$ term.

The CMB term can be expressed as an average over pixel of the correlation between the Q and U CMB signals. Here we focus on the case where the effective mixing matrix $\mathbf{\Lambda}_p$ and the noise covariance matrix \mathbf{N}_p are both pixel independent. We can then rewrite Eq. 9 as:

$$\langle S \rangle = -\text{tr} \left\{ (\mathbf{N}^{-1} - \mathbf{P}) \left(n_{\text{pix}} \mathbf{N} + \hat{\mathbf{\Lambda}}^{\text{cmb}} \left(\sum_p \langle \hat{s}_p^{\text{cmb}} \hat{s}_p^{\text{cmb},t} \rangle \right) \hat{\mathbf{\Lambda}}^{\text{cmb},t} + \hat{\mathbf{\Lambda}}^{\text{fg}} \sum_p \hat{s}_p^{\text{fg}} \hat{s}_p^{\text{fg},t} \hat{\mathbf{\Lambda}}^{\text{fg},t} \right) \right\} \quad (13)$$

$$= -\text{tr} \left\{ n_{\text{pix}} (\mathbf{N}^{-1} - \mathbf{P}) \left(\mathbf{N} + \hat{\mathbf{\Lambda}}^{\text{cmb}} \mathbf{S}^{\text{cmb}} \hat{\mathbf{\Lambda}}^{\text{CMB},t} + \hat{\mathbf{\Lambda}}^{\text{fg}} \mathbf{F} \hat{\mathbf{\Lambda}}^{\text{fg},t} \right) \right\} \quad (14)$$

where n_{pix} is the total number of observed pixels over

which the summation acts. Note that in the context of

cosmic birefringence the $\mathcal{B}(\beta_b)$ matrix has no effect on the foreground signals so $\mathbf{s}_p^{\text{fg}} \equiv \mathbf{c}_p^{\text{fg}}$. We use the pixel averages of the CMB sky component as \mathbf{S}^{cmb} and of foregrounds components as \mathbf{F} :

$$\mathbf{S}^{\text{cmb}} \equiv \frac{1}{n_{\text{pix}}} \sum_p \langle \hat{\mathbf{s}}_p^{\text{cmb}} \hat{\mathbf{s}}_p^{\text{cmb},t} \rangle \quad (15)$$

$$\mathbf{F} \equiv \frac{1}{n_{\text{pix}}} \sum_p \hat{\mathbf{s}}_p^{\text{fg}} \hat{\mathbf{s}}_p^{\text{fg},t} \quad (16)$$

Only the projection matrix \mathbf{P} needs to be updated when exploring the likelihood, Eq. 14, which makes it more efficient to explore the parameter space $\{\Gamma\}$.

However, depending on the number and specific nature of instrumental and foreground parameters considered in the problem, some degeneracies between the parameters may arise, preventing a robust determination of at least some of them. To deal with those, prior knowledge on some parameters may be required. They can come from instrumental calibration for instance. We allow for priors on the miscalibration angles, $\{\alpha_i\}$, and assume them to be Gaussians with a mean, $\tilde{\alpha}_i$, corresponding to the value of the parameter as measured during the calibration campaign and the dispersion, σ_{α_i} , reflecting the error of the measurement. This can be straightforwardly generalised to other parameters. The complete log-likelihood is then given by:

$$S' \equiv \langle S \rangle + \sum_{\alpha_i} \frac{(\alpha_i - \tilde{\alpha}_i)^2}{\sigma_{\alpha_i}^2}. \quad (17)$$

The log-likelihood without any priors, i.e., as in Eq. 14, is sufficient to constrain the foreground parameters as well as relative miscalibration angles of all the channels with respect to some reference angle. The reference angle (for instance, a polarisation angle of a selected channel) is the only degenerate parameter of the problem, which needs to be constrained with help of the priors. The constraints set by $\langle S \rangle$ on the relative miscalibration errors are tight as compared to the realistic current priors. They arise due the fact that the mixing matrix assumed in our data model, Eq. 2, combines the sky components for each Stokes parameter separately and therefore can not account for relative rotations between the channels, which unavoidably mix Q and U signals and do so differently for different channels. Any such mixing therefore constrains the relative angles. Consequently, the constraints on the relative miscalibration angles can be expected to be tight and largely independent of those on the foreground parameters. In contrast, a global rotation applied to all frequency channels can not be constrained as it merely corresponds to a similar rotation of the sky components.

In the presence of the priors the constraints on the relative angles are provided by the weighted average of the internal constraints and those provided by the priors. As the priors are centred at the measured, and thus

in general not the true values, of the parameters, this may lead to biased estimates. In cases studied here, the internal constraints dominate and the effect is typically small. Neglecting the prior constraints on the relative angle may be therefore beneficial in some circumstances and come at the cost of only minor increase of the statistical error. The priors then could be used to constrain solely the overall offset.

An important upshot of these observations is that thanks to the tight constraints on relative angles set by the data themselves, a single prior, i.e., on a single frequency channel, is sufficient to constrain the reference angle, thus allowing to solve the problem entirely, including setting cosmological constraints. A corollary of this is that if the priors on more frequency channels are available, they will lead to a better constraint on the reference angle and thus improve the cosmological constraints at the end. We will validate all these expectations using our results in the follow-up sections.

In the following we will assume that our priors are unbiased in a sense that if multiple calibration campaigns were to be performed the best-fit values obtained from each measurement will be drawn from a Gaussian with the mean corresponding to the true value of the parameter and the dispersion set by the measurement error. We will then average our likelihood over ensemble of the calibration procedures. The effective log-likelihood we will use hereafter therefore reads,

$$S' \equiv \langle S \rangle + \sum_{\alpha_i} \frac{(\alpha_i - \hat{\alpha}_i)^2}{2\sigma_{\alpha_i}^2}. \quad (18)$$

We also note that the split of the parameters into the relative angles and the reference angle, while convenient for getting better insights about the resulting constraints and degeneracies, is not necessary for actual implementation of the formalism where we can directly use the angles for each channel knowing that they are all well constrained if at least one prior is present.

2. Residuals

For each set of sampled spectral and instrumental parameters Γ we compute the effective mixing matrix $\mathbf{\Lambda}$ and use it to get the estimate of the separated sky components,

$$\begin{aligned} \mathbf{m}_p &= (\mathbf{\Lambda}^t \mathbf{N}^{-1} \mathbf{\Lambda})^{-1} \mathbf{\Lambda}^t \mathbf{N}^{-1} \mathbf{d}_p \\ &\equiv \mathbf{W}_p \mathbf{d}_p = \mathbf{W}_p \hat{\mathbf{\Lambda}} \hat{\mathbf{s}}_p + \mathbf{n}_p. \end{aligned} \quad (19)$$

The sought-after CMB map corresponds then to the first element of the sky component estimates, \mathbf{m} . The latter provides an unbiased (over the statistical ensemble of noise realisations) estimate of the true sky components if $\mathbf{W}_p \hat{\mathbf{\Lambda}} = \mathbf{1}$ for all pixels p . This will be in general only true if $\mathbf{\Lambda} = \hat{\mathbf{\Lambda}}$ (and in the case where we consider the ensemble average). So case-by-case, the estimates of

the sky components may include contributions from the other ones. Hereafter we refer to these as residuals.

We split the component vector, \mathbf{s} , the mixing matrix, $\mathbf{\Lambda}$, and the map-making operator, \mathbf{W}_p into a CMB and foreground parts. For \mathbf{W}_p the split is performed row-wise. We can then express noise-free CMB map estimate as:

$$\mathbf{s}_p^{\text{cmb}} = \mathbf{W}^{\text{cmb}} \left(\hat{\mathbf{\Lambda}}^{\text{cmb}} \hat{\mathbf{s}}_p^{\text{cmb}} + \hat{\mathbf{\Lambda}}^{\text{fg}} \hat{\mathbf{s}}_p^{\text{fg}} \right) \quad (20)$$

Note again that here \mathbf{s}^{cmb} has two elements corresponding to Stokes parameters.

As highlighted by Eq. 20, there are two types of effects which affect the estimation of the CMB map:

- A **multiplicative effect** coming from the action of $\mathbf{W}^{\text{cmb}} \hat{\mathbf{\Lambda}}^{\text{cmb}}$ on $\hat{\mathbf{s}}_p^{\text{cmb}}$. Without miscalibration $\mathbf{W}^{\text{cmb}} \hat{\mathbf{\Lambda}}^{\text{cmb}}$ would be the identity. However, this is not so here due to the action of the instrumental response matrix \mathbf{X} . Consequently, and unlike in Stompor *et al.* [40], in our case not all the actual CMB signal is bound to end up in the CMB map estimate. Instead, part of it may leak to the estimates of the other components and the CMB signal found in the CMB estimate may be corrupted.
- An **additive effect** coming from the contamination of foregrounds in $\mathbf{W}^{\text{cmb}} \hat{\mathbf{\Lambda}}^{\text{fg}} \hat{\mathbf{s}}_p^{\text{fg}}$ which is closely related to the usual definition of residuals in the context of parametric component separation.

Both these effects will in general give rise to a residual in the recovered CMB map either by adding some spurious foreground signal – the additive effect – or by directly misestimating the CMB signal – the multiplicative effect. This residual can subsequently potentially bias the estimation of cosmological parameters. We note that due to the presence of the multiplicative effect, related to the inclusion of the instrumental effects, the expression for the residual becomes more complex in our case that it was in the original formalism of [40], see, e.g., [39]. This can potentially make a direct generalisation of that formalism more cumbersome. In the formalism proposed hereafter we therefore do not perform Taylor expansion of the residuals with respect to the parameters. Instead, while computing the data matrix, we compute analytically only the term due to the multiplicative effect while the additive effect is computed numerically as in Eq 20 for each sample of instrumental and foreground parameters and averaging over these is performed with help of sampling of the spectral likelihood. This simplifies the formalism significantly and makes no assumption that the errors on spectral parameters derived from the spectral likelihood are small. A possible downside of this approach is that we lose some insight into the morphology and sources of the residuals.

C. Cosmological Parameter Estimation

We use the cleaned and corrected CMB map obtained in the previous step, Eq. 19, in order to estimate the cosmological parameters that we are interested in. This is performed with help of the cosmological likelihood. The estimated CMB maps comprise of multiple contributions as detailed in Eq. 20. This expression allows us to characterise the statistical properties of the CMB maps averaged over the ensemble of CMB and noise realisations, which include the effects due to the component separation. These are then used to construct the ensemble averaged cosmological likelihood, which is subsequently used to derive forecasts concerning cosmological parameters.

In the follow-up sections we detail the procedure and mathematical framework in the most general case and only in the last part of this section we specialise the formalism to the case of the joint estimation of the tensor-to-scalar ratio, r , and the cosmic birefringence angle, β_b .

1. CMB Data in Harmonic Domain

We build the cosmological likelihood in the harmonic domain as this is convenient for the purpose of the forecasting pipeline. However, the analogous constructions can be performed in the pixel domain as could be more appropriate for actual, case-by-case applications of the procedure. In the harmonic domain, the true sky components are represented by vectors of harmonic expansion coefficients and are denoted as $\mathbf{a}_j^{\text{comp}}$, true sky components are $\hat{\mathbf{a}}_j^{\text{comp}}$, where j is related to the multipole numbers (ℓ, m) as $j \equiv \ell^2 + \ell + m$. We collect the harmonic coefficients vectors for all the foreground components in a single vector denoted, \mathbf{a}^{fg} . The CMB signal estimate in the harmonic domain after the generalised component separation is then computed *case by case* for each set of values of Γ , e.g., a sample from the generalised spectral likelihood as in the formalism described here, is given by:

$$\mathbf{a}_j^{\text{cmb}} = \mathbf{W}^{\text{cmb}} \hat{\mathbf{\Lambda}}^{\text{cmb}} \hat{\mathbf{a}}_j^{\text{cmb}} + \mathbf{W}^{\text{cmb}} \hat{\mathbf{\Lambda}}^{\text{fg}} \hat{\mathbf{a}}_j^{\text{fg}} + \mathbf{W}^{\text{cmb}} \hat{\mathbf{a}}_j^{\text{noise}} \quad (21)$$

Our cosmological likelihood is averaged over the CMB and noise realisations and therefore uses the covariance of the recovered CMB map data after generalised component separation defined as $\mathbf{E}_{jj'} \equiv \langle \mathbf{a}_j \mathbf{a}_{j'}^t \rangle$. Using Eq. 21 and assuming that there is no cross-correlations between $\mathbf{a}_j^{\text{cmb}}$, \mathbf{a}_j^{fg} and $\mathbf{a}_j^{\text{noise}}$, we get:

$$\begin{aligned} \mathbf{E}_{jj'} &= \mathbf{W}^{\text{cmb}} \hat{\mathbf{\Lambda}}^{\text{cmb}} \mathbf{C}_\ell^{\text{cmb}} \delta_{jj'} \hat{\mathbf{\Lambda}}^{\text{cmb},t} \mathbf{W}^{\text{cmb},t} \\ &+ \mathbf{W}^{\text{cmb}} \hat{\mathbf{\Lambda}}^{\text{fg}} \hat{\mathbf{a}}_j^{\text{fg}} \hat{\mathbf{a}}_{j'}^{\text{fg},t} \hat{\mathbf{\Lambda}}^{\text{fg},t} \mathbf{W}^{\text{cmb},t} \\ &+ \mathbf{C}_\ell^{\text{noise}} \delta_{jj'} \end{aligned} \quad (22)$$

where $\mathbf{C}_\ell^{\text{cmb}} \equiv \frac{1}{2\ell+1} \sum_m \langle \hat{\mathbf{a}}_j^{\text{cmb}} \hat{\mathbf{a}}_j^{\text{cmb},t} \rangle$, and $\mathbf{C}_\ell^{\text{noise}}$ is detailed in the next section. As we used the output fre-

quency maps of PySM for the foregrounds signal, $\hat{\mathbf{a}}_j^{\text{fg}}$ is not affected by the averaging over noise and CMB realisations.

Since the sky signal objects $\mathbf{s}_p^{\text{comp}}$ used to compute $\mathbf{a}_j^{\text{comp}}$ contained Q & U polarisation information the resulting $\mathbf{C}_\ell^{\text{cmb}}$, $\mathbf{C}_\ell^{\text{noise}}$ power spectra contain E and B auto and cross-spectra. The $\hat{\mathbf{a}}_j^{\text{fg}} \hat{\mathbf{a}}_{j'}^{\text{fg},t}$ matrix contains products of all multipole coefficients of polarised foreground component. Computing those may pose a significant challenge as they may depend on fine details of the foreground models. However, as discussed in [40] and shown below, in the computation of the likelihood we in fact only need the auto- and cross- spectra of all foreground signals. These are generally known much better and our predictions are consequently more robust.

The first term of $\mathbf{E}_{jj'}$ depends explicitly on \mathbf{W}^{cmb} reflecting the effect of the estimation of the instrumental parameters in the generalised likelihood on the CMB content in the estimated CMB signal. As mentioned earlier, see [40], in the case without instrumental effects, $\mathbf{W}^{\text{cmb}} \mathbf{A}^{\text{cmb}} = \mathbf{1}$, the first term of $\mathbf{E}_{jj'}$ would reduce to $\mathbf{C}_\ell^{\text{cmb}} \delta_{jj'}$. The instrumental parameters also affect the second term of Eq. 22. This term produces a non-vanishing contribution even in the absence of these, which is however modified if they are present.

The last term concerns the noise power spectra $\mathbf{C}_\ell^{\text{noise}}$. This is the noise in the CMB map obtained after generalised component separation:

$$\begin{aligned} \mathbf{C}_\ell^{\text{noise}} &= \mathbf{W}^{\text{cmb}} \frac{1}{2\ell+1} \sum_m \langle \hat{\mathbf{a}}_j^{\text{noise}} \hat{\mathbf{a}}_j^{\text{noise},t} \rangle \mathbf{W}^{\text{cmb},t} \\ &= \left[(\boldsymbol{\Lambda}^t \mathbf{N}_\ell^{-1} \boldsymbol{\Lambda})^{-1} \right]_{\text{cmb} \times \text{cmb}} \end{aligned} \quad (23)$$

where \mathbf{N}_ℓ for the frequency band i is computed using the formula and the Simons Observatory SAT's $1/f$ power index [9]:

$$\mathbf{N}_\ell^i \equiv (w_i)^{-1} e^{\left(\ell(\ell+1) \frac{\text{FWHM}_i^2}{8 \log 2} \right)} \left(\left(\frac{\ell}{\ell_{knee}^i} \right)^{-2.4} + 1 \right) \quad (24)$$

with w_i^{-1} the sensitivity of the frequency channel i in μK^2 . Here we also take into account the effect of the beam and inserted it by hand since, as mentioned in [40], for simplicity in the generalised spectral likelihood the noise is assumed to be white-like all the way down to the pixel scale and no beams are accounted for. Here, FWHM_i stands for the full-width half maximum for the i channel, in radians. $1/f$ noise is also included via the last term and ℓ_{knee}^i is the position of the knee in harmonic space for the i^{th} frequency band. We have assumed no frequency to frequency correlations here.

2. Covariance Matrix

Now that we have all the terms that compose our recovered CMB data in harmonic domain. We can build

the model that will enter our cosmological likelihood in the form of the covariance matrix \mathbf{C} . First we include the covariance matrix modelling the CMB power spectra as a function of the cosmological parameters $\{\theta\}$ that we want to estimate. In this general approach the CMB model covariance matrix $\mathbf{C}_\ell^{\text{cmb,model}}$ can contain E/B auto and cross-spectra. We add our model for the instrumental noise as well and this gives:

$$\mathbf{C}_{jj'} = \mathbf{C}_\ell^{\text{cmb,model}}(\theta) \delta_{jj'} + \mathbf{C}_\ell^{\text{noise}} \delta_{jj'} \quad (25)$$

In the case of joint birefringence angle β_b and tensor-to-scalar ratio estimation r , $\mathbf{C}_\ell^{\text{cmb,model}}$ reads:

$$\begin{aligned} &\mathbf{C}_\ell^{\text{cmb,model}}(r, \beta_b) \\ &\equiv \mathcal{R}(\beta_b) \begin{pmatrix} C_\ell^{EE,p} & 0 \\ 0 & r \cdot C_\ell^{BB,p} + A_L \cdot C_\ell^{BB,\text{lens}} \end{pmatrix} \mathcal{R}^{-1}(\beta_b) \end{aligned} \quad (26)$$

Where $C_\ell^{XY,p}$ are the primordial CMB power spectra and $C_\ell^{BB,p}$ is computed for $r = 1$. $C_\ell^{BB,\text{lens}}$ is the lensed B mode power spectrum. A_L encodes the delensing where $A_L = 1$ means no delensing and $A_L = 0$ means total delensing. In the following we only consider $A_L = 1$. We assumed here that the *primordial* CMB EB cross spectra is null. Models predicting non-zero primordial EB could be accounted for here in the covariance matrix, but we choose to ignore such models for simplicity and leave it for future work. We also ignore the effect of r on the EE power spectrum. We can then finally input our model and data in the cosmological likelihood which is computed case by case for each set of Γ parameters drawn from the generalised spectral likelihood distribution, e.g. Tegmark *et al.* [44]:

$$\begin{aligned} \langle S^{\text{cos}} \rangle &= \text{tr} \mathbf{C}^{-1} \mathbf{E} + \ln \det \mathbf{C} \\ &= f_{\text{sky}} \sum_{\ell=\ell_{\min}}^{\ell_{\max}} \frac{(2\ell+1)}{2} \left(\text{Tr}(\mathbf{C}_\ell^{-1} \mathbf{E}_\ell) + \ln(\det(\mathbf{C}_\ell)) \right), \end{aligned} \quad (27)$$

where,

$$\mathbf{E}_\ell \equiv \frac{1}{2\ell+1} \sum_m \mathbf{E}_{jj}, \quad \text{and } j = \ell^2 + \ell + m. \quad (28)$$

This shows that we only need to know m -averaged, diagonal elements of the data matrix, \mathbf{E} , which are fully defined by the cross-spectra of all the foreground signals as well as the CMB power spectra. We note that this conclusion as well as Eq. 27 hold only if the noise is isotropic.

D. Implementation

The overall implementation of the method follows its main stages as described in the introduction of

this section and as shown in Fig 2 in the case of the forecasting framework. Here, we provide a few more details concerning the implementation of some of the key stages for each of the two steps of the method.

First step: We need to estimate \mathbf{S}^{cmb} , \mathbf{F} (defined in Eq 15 and Eq 16 respectively) and \mathbf{N} for the CMB, foreground and noise signals. Those values are averaged over observed sky pixels as well resulting in a 2×2 matrix encoding QQ, UU and QU correlations only. Here we are focusing on polarised signal only but it could be easily generalised to intensity signal as well. In practice to get \mathbf{S}^{cmb} we average 1000 CMB map realisations generated using the `synfast` function in `healpy`² [45, 46] and using as a template a power spectra generated by `CAMB`³ using the cosmological parameters estimated in the Planck 2018 release [47], with $\ell_{\text{min}} = 0$ and $\ell_{\text{max}} = 4000$. The details of the resolution and sky coverage used depend on the experiment chosen for the forecast, similarly for \mathbf{N} . The cosmological values are also left as a choice in the case of this forecast. The experiment and cosmological parameters chosen are detailed in section IV.

For the foregrounds signal \mathbf{F} we rely on noiseless frequency maps given by `PySM` [48] that we use to perform the averaging over observed pixels. Once again the details for the experimental characteristics and foreground models complexity are detailed in the next section.

The component separation code used here is heavily based on the `ForeGroundBuster (FGBuster)` library⁴ and has been adapted to account for systematic effects such as polarisation angles and the addition of priors as mentioned earlier.

The sampling of the generalised spectral likelihood is performed using the `emcee` package [49]. We used 2 walkers per dimensions, with 13,000 steps and we burned the 5,000 first ones (for the fiducial SO SAT case explored in this paper with 6 miscalibration angles and 2 foreground parameters it totals 128,000 samples).

Second step: For the construction of the observed and model CMB power-spectra $\mathcal{C}_\ell^{\text{cmb}}$ we use the same Planck CMB power spectra templates as the one used for the generation of CMB maps in the first step and simulations. For the harmonic decomposition of the foregrounds in the data \mathbf{a}_j^{fg} again we use the same frequency maps coming from `PySM` as in the first step. However to compute the power spectra we need also to take possible correlations between frequencies into account, so for each frequency map we compute the corresponding $a_{\ell m}$ using the `map2alm` function in `healpy` and then we compute the power spectra for each possible combination. This operation can be a bit costly but

since the frequency maps given by `PySM` are not random it has to be done only once per foreground model and instrument parameters.

Similarly as in the first step we are only using polarised power spectra EE, BB and EB but one could easily add T auto and cross-spectra.

To understand the statistical impact of the first step on the estimation of cosmological parameters we want to map the distribution of the $\gamma \in \Gamma$ parameters on the cosmological parameters. To do so we compute for each sample (after burning) of the spectral likelihood the resulting data correlation matrix \mathbf{E}_ℓ following Eq. 22. We want to draw one sample from the corresponding cosmological likelihood Eq. 27. To avoid any bias coming from initial values we use once again `emcee` with 300 steps and a burn of 299 so that we only keep the last point. So finally for each point of the sampling of the spectral likelihood corresponds a point in the cosmological parameter space.

IV. APPLICATION

In this section we discuss the application of the forecasting method described in the previous section. We focus here on the case of a typical CMB ground-based telescope of third generation demonstrating the proposed framework and its performance on a specific experimental set-up as described in the next section. The framework is however general and can be applied to any other CMB experiment. Below we first describe the instrument configuration, followed by the sky simulation used in the application and finally the specific analysis assumptions that we consider in this work, such as the modelling of the instrumental response matrix \mathbf{X} .

A. Instrument specifications

For concreteness we use the configuration and noise specifications of the upcoming Simons Observatory's (SO) Small Aperture Telescopes (SAT) as described in [9]. The three SO SATs are planned to observe the sky in 6 frequency channels: 27, 39, 93, 145, 225 and 280 GHz. This will help to separate the CMB signal from the astrophysical foregrounds.

The SATs will observe $f_{\text{sky}} \approx 10\%$ of the sky and generate sky maps with a typical resolution of $n_{\text{side}} = 512$ which corresponds to ~ 6.8 arcmin using the `HEALPix` convention [45, 46]. This results in around 3×10^5 observed sky pixels. Given the resolution, sky coverage and noise property we fix the multipole scales at $\ell_{\text{min}} = 30$ and $\ell_{\text{max}} = 300$.

We use the publicly available code `V3calc`⁵ and the sensi-

² <http://healpix.sf.net>

³ <https://camb.info>

⁴ <https://github.com/fgbuster/fgbuster>

⁵ https://github.com/simonsobs/so_noise_models

Frequency channel [GHz]	27	39	93	145	225	280
sensitivity ^a [$\mu\text{K-arcmin}$]	21	13	3.4	4.3	8.6	22
ℓ_{knee}	15	15	25	25	35	40
FWHM [arcmin]	91	63	30	17	11	9

^a The quoted numbers give anticipated SAT white noise levels in temperature. To get Q and U sensitivities a $\sqrt{2}$ multiplicative factor must be applied.

TABLE II. SO SAT baseline white noise levels, optimistic $1/f$ noise properties, and FWHMs.

tivities from the SO science goals and forecast paper [9] to compute the sensitivity per frequency w_i after five years of observation for the high frequencies focal plane (225 and 280 GHz), 5 and 4 years for two middle frequencies focal planes (93, 145 GHz), and 1 year of observation for the low frequencies focal plane (27, 39 GHz). The baseline white noise case used is detailed in II. This gives us the noise per sky pixel and per frequency band i : \mathbf{N}_p^i used in Eq. 11:

$$\mathbf{N}_p^i = w_i^{-1} \quad (29)$$

Where the noise covariance is assumed to be white-like and therefore uncorrelated between pixels and frequencies. Forgetting about pixel-pixel correlations in \mathbf{N}_p turns out to be a reasonable assumptions given the latest available SO simulations [50].

As mentioned previously for the cosmological likelihood we take into account beam effects and $1/f$ noise in Eq. 24. For the computation of \mathbf{N}_ℓ^i we use the baseline sensitivity and so-called optimistic $1/f$ modes of SO SAT, as well as the SAT's beams as detailed in table II.

B. Input Sky Simulations

1. Foregrounds

For foreground maps we use sky signals generated by PySM [48].

The fiducial foreground case we use is the “d0s0” model. For dust, this corresponds to a modified black-body parameterised by its spatially-constant temperature T_d and spectral index β_d . The synchrotron emissions is modeled as a power law characterised by the constant spectral index β_s . The spectral emission densities for those two components are expressed as:

$$Y_{\text{sync,p}}(\nu, \beta_s) = Y_{\text{sync,p}}(\nu_{0,s}) \left(\frac{\nu}{\nu_{0,s}} \right)^{\beta_s} \quad (30)$$

$$Y_{\text{dust,p}}(\nu, \beta_d, T_d) = Y_{\text{dust,p}}(\nu_{0,d}) B(\nu, T_d) \left(\frac{\nu}{\nu_{0,d}} \right)^{\beta_d} \quad (31)$$

Where Y can be a Q or U map of a component, expressed in MJy/sr. $Y_{\text{sync,p}}(\nu_{0,s})$ and $Y_{\text{dust,p}}(\nu_{0,d})$ are the template maps for synchrotron and dust at their respective reference frequencies $\nu_{0,s} = 23$ GHz and $\nu_{0,d} = 353$

GHz that are then scaled at the frequencies of interest for observations. $B(\nu, T_d)$ is a black body at temperature T_d and frequency ν . In the PySM “d0s0” simulation, the spatially constant spectral parameters are based on Planck results [51] and are given by:

$$\beta_d = 1.54, \quad T_d = 20\text{K}, \quad \beta_s = -3. \quad (32)$$

For more complex foregrounds we also use the “d1s1” model which considers spatially varying $\beta_d(p)$, $T_d(p)$ and $\beta_s(p)$.

We used “d7s3” as well, where “s3” describes the synchrotron using a power law curved by a curvature term \mathcal{C} constant over the sky:

$$Y_{\text{sync,p}}(\nu, \beta_s) = Y_{\text{sync,p}}(\nu_{0,s}) \left(\frac{\nu}{\nu_{0,s}} \right)^{\beta_s(p) + \mathcal{C} \ln(\nu/\nu_0)} \quad (33)$$

“d7” uses as a template the same 353 GHz map as “d1” but the frequency scaling used is based on dust grain models with different physical properties, shape, size, temperature described in detail in [52, 53]. This model does not have an analytic function to describe the frequency scaling of the dust template and is therefore a good benchmark to test the parametric component separation since it does not trivially conform with the assumptions of the method.

2. CMB

For the CMB we set all the parameters to the values constrained by Planck [54] and only vary two parameters, the tensor-to-scalar ratio r and the birefringence angle β_b . We do not consider delensing in this work, i.e. $A_L = 1$ in Eq. 26. However this can be straightforwardly included in our framework. The input CMB power spectra used to get the frequency maps (as described in the previous section) are computed using the same equation as the model CMB in Eq. 26. We choose two sets of cosmological parameters in addition to the fiducial ΛCDM cosmological parameters from Planck 2018 [54]:

$$r = 0.0, \quad \beta_b = 0.0^\circ \quad (34)$$

$$r = 0.01, \quad \beta_b = 0.35^\circ \quad (35)$$

With $\beta_b = 0.35^\circ$ corresponding to the central value found in the work of Minami and Komatsu [18].

3. Instrumental Effects

In the simulation we consider the effect of a potential miscalibration of the polarisation angle of each of the frequency bands of the telescope. We model this effect assuming that each frequency channel has its own independent polarisation angle. This assumption can be adjusted as needed: our approach is generalisable to a

miscalibration angle per focal plane, one per wafer, one per pixels, etc. In this work we use the input miscalibration angles summarised in Table III. But the presented results do not significantly depend on the specific values assumed.

Frequency channel [GHz]	27	39	93	145	225	280
Input polarisation angle [°]	1	1.66	2.33	3	3.66	4.33

TABLE III. Input polarisation angle per frequency bands

C. Analysis Hypotheses and Priors

The actual mixing matrix assumed for modelling the data and therefore used in the minimisation of the spectral likelihood does not need to correspond to the one used to generate the data themselves. A mismatch between the two would however lead to a bias in the spectral, instrumental and possibly cosmological parameter estimation. This has been discussed, in the specific case of spectral indices, in Stompor *et al.* [40].

In the model used in the analysis, both dust and synchrotron parameters are assumed constant over the sky. This is the simplest option which is also in line with what is currently performed in the SO analysis [9]. In the case of SO SATs we fix dust temperature to $T_d = 20\text{K}$ as suggested by Planck results [51] and in agreement with the “d0s0” assumption, Eq. 32, we do so because the SATs do not have enough high frequency observation bands to discriminate between T_d and β_d . Consequently, we model the data with the two spectral indices β_d and β_s , assumed to be the same for all considered sky pixels.

This model provides only an accurate description of the data simulated using the “d0s0” model of PySM, but not those obtained for “d1s1” and “d7s3” models, allowing us to explore the effects of the mismatch between the assumed and actual mixing matrix on the cosmological parameter estimation. For the instrumental matrix \mathbf{X} we assume an isotropic rotation of the polarisation angle for each of the frequency, exactly as for the sky simulations.

As seen in Eq. 18 we add Gaussian priors to the spectral likelihood. Throughout this work we add priors with a precision $\sigma_{\alpha_i} = 0.1^\circ$ on one or several frequency channels as detailed in section V. This corresponds to the precision goal for the drone calibrator developed for SO [28]. Unless specified otherwise the priors are centred at the true input polarisation angles. We will also explore the evolution of cosmological parameters estimation with respect to prior precision and, conversely, the required calibration precision to achieve scientific goals.

V. RESULTS

First we present the results of the first analysis step that retrieves the spectral indices and the miscalibration angles from noisy, foreground-contaminated and miscalibrated frequency maps. Then we present the results of the second step that constrains cosmological parameters. We discuss various examples to demonstrate the effects of the different contaminants on the cosmological parameters estimation, such as biases or precision loss. Afterwards we present the evolution of the constraint on cosmological parameter as a function of prior precision. And finally we explore the case where calibration priors are biased and their impact on instrumental and cosmological parameters estimations.

A. Fiducial Case: “d0s0”, $r = 0$, $\beta_b = 0^\circ$

We start with the simplest case of the “d0s0” PySM model that assumes constant foreground spectral parameters across the sky. The mixing matrix \mathbf{A} , Eq. 4 that we use throughout this work has been constructed using the same assumptions and so should match with the input foreground maps.

We explore two cases, one with a prior on each frequency channel and the other with a prior on the 93 GHz channel only. In both cases the prior precision is $\sigma_{\alpha_i} = 0.1^\circ$.

1. Prior on a Single Channel

First we consider a prior on the 93 GHz channel only with a precision of $\sigma_{\alpha_{93}} = 0.1^\circ$. We choose this channel as it is the one with the most CMB signal and where most of the calibration effort is currently being deployed.

a. Generalised Spectral Likelihood Results:

As described in the paragraph IIID we first perform a MCMC sampling of the generalised spectral likelihood, Eq. 18.

The corresponding results are shown in Fig. 7 where the orange contours are obtained from the MCMC samples, the purple dashed line represents the Gaussian prior on the 93 GHz channel and the grey dashed lines the input parameters. The $1-\sigma$ statistical errors of the parameter estimations are detailed in Table IV.

We notice that with only one prior on one polarisation angle we are able to have an unbiased estimate for all 6 polarisation angles and 2 spectral indices. Indeed the fact that we use all 6 frequency maps simultaneously in the generalised spectral likelihood and in particular the fact that the effective mixing matrix $\mathbf{\Lambda}$ relates all frequency bands through the stiff frequency scaling laws propagates the calibration information from one prior to the other frequency channels. In essence the prior here sets the “global” polarisation angle of the system and the

Foreground input	“d0s0”		“d1s1”		“d7s3”	“d0s0” *
Number of priors	1	6	1	6	6	6
$\alpha_{27} [^\circ]$	1.0 ± 0.2	1.00 ± 0.08	1.0 ± 0.2	1.01 ± 0.08	1.01 ± 0.08	1.00 ± 0.08
$\alpha_{39} [^\circ]$	1.7 ± 0.1	1.67 ± 0.05	1.7 ± 0.1	1.67 ± 0.05	1.67 ± 0.05	1.67 ± 0.05
$\alpha_{93} [^\circ]$	2.3 ± 0.1	2.33 ± 0.05	2.3 ± 0.1	2.33 ± 0.05	2.33 ± 0.05	2.33 ± 0.05
$\alpha_{145} [^\circ]$	3.0 ± 0.1	3.00 ± 0.05	3.0 ± 0.1	3.00 ± 0.05	3.00 ± 0.05	3.00 ± 0.05
$\alpha_{225} [^\circ]$	3.7 ± 0.1	3.67 ± 0.05	3.7 ± 0.1	3.66 ± 0.05	3.66 ± 0.05	3.66 ± 0.05
$\alpha_{280} [^\circ]$	4.3 ± 0.1	4.33 ± 0.06	4.3 ± 0.1	4.33 ± 0.06	4.33 ± 0.06	4.33 ± 0.06
β_d	1.540 ± 0.007	1.540 ± 0.007	1.575 ± 0.008	1.575 ± 0.007	1.377 ± 0.007	1.540 ± 0.007
β_s	-3.000 ± 0.009	-3.000 ± 0.009	-3.006 ± 0.009	-3.006 ± 0.009	-3.046 ± 0.009	-3.000 ± 0.009
r	0.000 ± 0.002	0.000 ± 0.002	0.002 ± 0.002	0.002 ± 0.002	0.002 ± 0.002	0.010 ± 0.002
$\beta_b [^\circ]$	0.00 ± 0.1	0.00 ± 0.07	0.00 ± 0.1	0.00 ± 0.07	0.00 ± 0.07	0.35 ± 0.07

TABLE IV. Summary of results for different input foreground models and instrumental parameters. All the prior used here have the precision $\sigma_{\alpha_i} = 0.1^\circ$. * In the last column (“d0s0”) the input cosmological parameters are $r = 0.01$ and $\beta_b = 0.35^\circ$.

effective mixing matrix allows to retrieve all the relative polarisation angles between channels.

The accuracy with which we can estimate polarisation angles is limited by the prior precision as summarised in Table IV. The 93 GHz channel achieves the best precision on polarisation angle, $\sigma(\alpha_{93}) = 0.099^\circ$, which corresponds to the prior precision (within the accuracy provided by the sampling). All other channels show larger errors.

Furthermore we are able to retrieve the foreground spectral parameters with a precision comparable with the standard version of parametric component separation using FGBuster in SO without instrumental parameter estimation [9].

Their estimation is not biased by the generalisation of the spectral likelihood. With the unbiased estimation of instrumental and spectral parameters we can proceed to the next step: the estimation of cosmological parameters.

b. Cosmological Likelihood Results: As detailed in section IIID, for each sample of the spectral likelihood displayed in Fig. 7 we draw one sample of the corresponding cosmological likelihood.

This approach allows us to efficiently sample the full distribution. The result is shown in Fig. 3 where the orange contours are the MCMC samples obtained assuming a single 93 GHz prior, and the grey dash lines the input parameters. The estimations of both r and β_b are unbiased and with $r = 0.0002^{+0.0015}_{-0.0017}$ which is compatible with the SO SATs published forecasts [9], and $\sigma(\beta_b) = 0.11^\circ$ which is 10% bigger than the error bars expected from prior precision alone, which can be explained by the presence of noise and cosmic variance.

As a conclusion for this case with simple foreground SEDs that match our model, and with non-zero polarisation angles, it seems that the method leads to unbiased estimates of spectral and hardware parameters, and provides competitive results on r and an estimation of the birefringence angle β_b limited only by the prior precision, as one can naively expect.

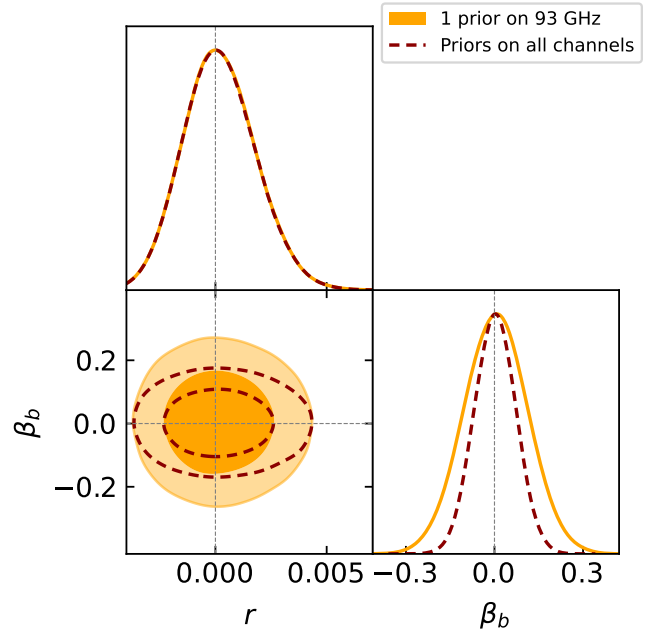


FIG. 3. Cosmological likelihood sampling, Eq. 27, after foreground cleaning and systematic effect correction with PySM “d0s0” as input and only *one* prior on the 93 GHz polarisation angle (orange). Dash dark-red contours correspond to the case with priors on all polarisation angles. The grey dash lines correspond to the input values. The central values and error bars are in Table IV.

2. Priors on All 6 Channels

We now investigate another case with priors on all 6 polarisation angles. We proceed in a similar fashion as in the previous case.

a. Generalised Spectral Likelihood Results: Fig. 8 shows the results of the MCMC sampling of the generalised spectral likelihood. Comparing the priors (dashed purple) and the samples (orange) we see that,

contrary to the previous case, the precision of the polarisation angle estimation is not limited by the prior precision. All error bars are significantly lower than the prior precision $\sigma_{\alpha_i} = 0.1^\circ$. It seems that the sharing of prior information from one channel to the other thanks to the mixing matrix and the stiff frequency scaling laws help constraining the polarisation angles with maximal precision.

b. Cosmological Likelihood Results: The distribution of cosmological parameters after the generalised component separation with 6 priors is presented as dark-red curves in Fig. 3. Again, the estimations of both r and β_b are unbiased and with a precision of $\sigma(r) \approx 2 \times 10^{-3}$ and $\sigma(\beta_b) \approx 0.07^\circ$ as mentioned in Table IV. The estimation of r is therefore unchanged with respect to the previous case but the estimation of β_b has improved as a consequence of the improvement of the polarisation angle estimation in the first step. Having polarisation angle calibration on multiple frequency bands would therefore improve $\sigma(\beta_b)$ without necessarily requiring a large improvement of the calibration precision itself which can be very challenging.

B. Complex Foregrounds, $r = 0$, $\beta_b = 0^\circ$

1. Spatially-Varying Foreground SEDs: “d1s1”

Now the foreground model used in the simulated *data* contains spatially-varying spectral indices.

Yet the model to build the mixing matrix still assumes constant spectral indices. Here we therefore assess the bias on cosmological parameters induced by the mismatch between foreground model and data.

For conciseness we focus on the case with *priors on all polarisation angles*. The results obtained with one 93 GHz prior are detailed in Table IV.

a. Generalised Spectral Likelihood Results:

Fig. 9 shows the results of the generalised spectral likelihood sampling. The estimation of polarisation angles are not significantly affected by the more complex foregrounds and results are similar to the previous, 6-priors, case. The spectral likelihood still manages to estimate an effective set of spectral indices. However they do not correspond to the reality of the data as the foreground indices are defined independently in each sky pixel.

b. Cosmological Likelihood Results: Results are shown in Fig. 4. The estimation of the birefringence angle β_b is not significantly affected by the complex foregrounds and by the mismatch between data and model. This seems consistent with the unbiased estimate of polarisation angles in the previous step, and the foreground leakage to the recovered CMB EB correlation seems under-control. For r the estimation is slightly biased with $r \sim 0.0016$ but it is still $1\text{-}\sigma$ compatible with the input, $r = 0$ value. The relatively small effects of foreground SEDs mismatch is mostly thanks to the small

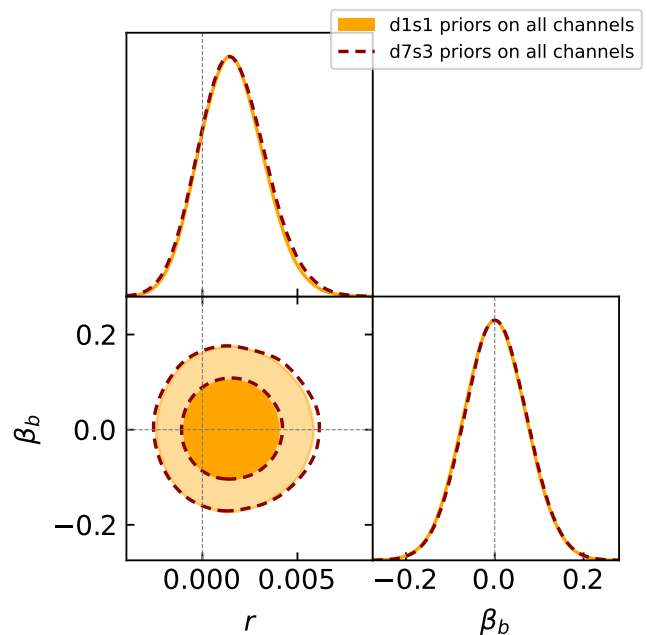


FIG. 4. Cosmological likelihood sampling after foreground cleaning and systematic effect correction with priors on *all* polarisation angles. Results obtained for *d1s1* (resp. *d7s3*) are shown as orange contours (resp. dash dark-red). The grey dash lines correspond to the input values.

sky fraction observed by SO SATs ($f_{sky} = 0.1$), their limited frequency coverage and their large angular scale, $\ell_{min} = 30$. Spatially varying spectral indices on e.g. a larger sky patch or with a larger frequency coverage would certainly bias more significantly both parameters.

2. Non-Parametric Dust Model and Curved Synchrotron: “d7s3”

As described in IV B 1 the “d7” dust model is highly non-parametric and should be a good way to push our generalised parametric component separation to its limits. The “s3” synchrotron model adds complexity as well with a global curvature term not taken into account in our mixing matrix. Polarisation angles do not seem affected by non-parametric input foregrounds as can be seen in Tab. IV. For the cosmological likelihood, once again the limited sky fraction used by SO SATs limits the impact of spatial variation and the generalised spectral likelihood sampling gives similar results as the “d1s1” case. The impact on the cosmological likelihood is therefore limited as well, as shown in Fig. 4 as dashed dark-red contours. The error bars are slightly different as described in Tab. IV with a $\sim 5\%$ increase in the upper error bar on r with respect to the “d1s1” case, and a $\sim 1.4\%$ decrease on $\sigma(\beta_b)$, and with no detectable biases.

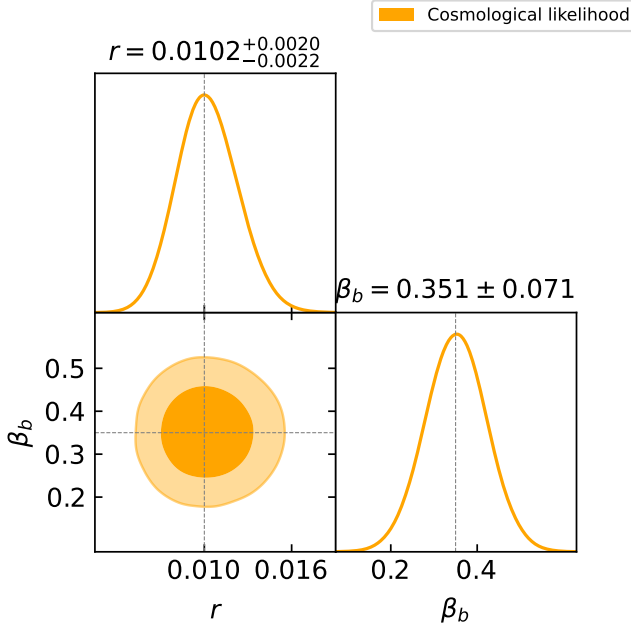


FIG. 5. Cosmological likelihood sampling after foreground cleaning and systematic effect correction with “d0s0” as foreground input and priors on *all* polarisation angles. Input cosmological parameters are $r = 0.01$ and $\beta_b = 0.35^\circ$. The grey dash lines correspond to the input values. This figure is analogous to Fig. 3 but assumes a non-zero birefringence angle.

C. Non-zero Cosmological Parameters: $r = 0.01$, $\beta_b = 0.35^\circ$, Simple Foregrounds “d0s0”.

For completeness we now focus on a case where cosmological parameters are non-zero, with the fiducial foreground model “d0s0” and priors on all channels. We do not show the result of the generalised spectral likelihood as they are similar to the one presented in Fig. 8.

Fig. 5 displays the cosmological constraints and indicates the possibility of detecting $r = 0.01$ with a $5\text{-}\sigma$ precision, consistent with previous forecast [9]. A $\sim 5\sigma$ detection of the $\beta_b = 0.35^\circ$ hinted by Planck data [17, 18] seems achievable as well. We do not present the results for “d1s1”, “d7s3” or with only one prior as they are analogous to the $r = 0$ and $\beta_b = 0^\circ$ cases presented previously.

For complex foregrounds the results on r are biased but within the $1\text{-}\sigma$ error bars and the results on β_b are unbiased with error bars going from 0.1° to 0.07° for the 1 and 6 priors cases respectively.

D. Cosmological Parameters Estimation as a Function of Prior Precision

To better understand the dependence of the results on the prior precision and on the number of priors we per-

form the previous analyses with several calibration precisions. We limit ourselves to the case where $r = 0$, $\beta_b = 0^\circ$, and using the simple “d0s0” foregrounds in the input data. We explore prior precision in the range $0.001^\circ \leq \sigma_{\alpha_i} \leq 5^\circ$. Both the case with 1 prior on the 93 GHz channel and the case with priors on all polarisation angles are considered. The evolution of $\sigma(\beta_b)$ with respect to σ_{α_i} is displayed in Fig. 6. The blue points correspond to the 1 prior case: it is clear that $\sigma(\beta_b)$ is strictly limited by the prior precision as it follows the $y = x$ line. However we also see that there are two regimes, the first when $\sigma_{\alpha_i} \gtrsim 0.05^\circ$ for which $\sigma(\beta_b)$ exactly follows the prior precision, and a second regime at $\sigma_{\alpha_i} \lesssim 0.05^\circ$ where the precision hits a plateau at $\sigma(\beta_b) \approx 0.045^\circ$. This plateau comes from cosmic and noise variances which dominate the error budget over the prior precision. A similar behaviour is observed in the 6 priors case. However, for large σ_{α_i} , $\sigma(\beta_b)$ follows a line parallel to the 1 prior case but shifted to lower values as the curve seem to follow roughly $y = x/\sqrt{\#prior}$. As we saw already in section V A 2, the method is able to combine multiple priors to give an overall better precision on β_b .

The cosmic and noise variance limited regime starts at a larger σ_{α_i} as well compared to the 1 prior case, but the level of the plateau is not affected as it is caused by noise and cosmic variance.

This result can help us with future calibration requirements and suggests that as long as we are in the first regime to achieve a given $\sigma(\beta_b)$ one must either improve the precision of the calibration method, or up to a certain limit depending on the number of channels, calibrate several frequency channels to get the same results. As improving the absolute precision of calibration is quite challenging, multiplying calibration campaigns to other frequency channels seems to be a reasonable option.

Furthermore to see how both noise and cosmic variance account for the level of the plateau we performed a *noiseless* analysis with 6 priors represented by the orange dots in the figure. The cosmic-variance limit reaches $\sigma(\beta_b) \approx 0.026^\circ$. This seems to indicate that for the sky coverage and noise levels of SO SATs the noise accounts for $\sim 42.2\%$ of the plateau’s amplitude. To improve on the latter one needs either to lower the noise or to increase f_{sky} . However with a larger sky survey the spatial variability of foreground SEDs will potentially become a bigger issue for the component separation and might bias the estimation of cosmological parameters.

E. Biased Priors

For now we only considered cases where the prior used were centred on the true values of miscalibration angles. Even though we assumed that we averaged our likelihood over an ensemble of calibration procedures leading to the effective log-likelihood in Eq. 18 it is still worth exploring how the framework performs with biased priors. In par-

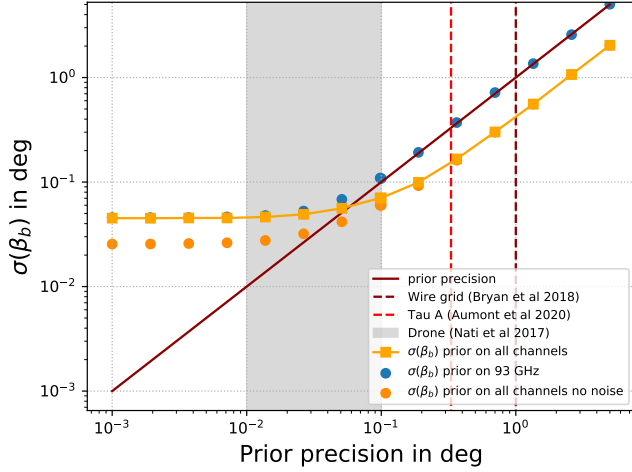


FIG. 6. Evolution of $\sigma(\beta_b)$ with respect to prior precision in different calibration and noise scenarios.

Input angle [°]	Input 1 prior [°]	Input 6 priors, equal biases [°]	Input 6 priors, different biases [°]
$\alpha_{27} = 1.00$		1.13 (0.13)	1.28 (0.28)
$\alpha_{39} = 1.67$		1.80 (0.13)	0.88 (−0.78)
$\alpha_{93} = 2.33$	2.46 (0.13)	2.46 (0.13)	2.46 (0.13)
$\alpha_{145} = 3.00$		3.13 (0.13)	3.30 (0.30)
$\alpha_{225} = 3.67$		3.80 (0.13)	5.12 (1.46)
$\alpha_{280} = 4.33$		4.46 (0.13)	4.43 (0.09)

TABLE V. The 3 different cases of biased prior centres used for each frequency channels. The numbers in parentheses correspond to the value of the bias in degrees. The last line points to the figure corresponding to the spectral likelihood sampling for each case.

particular to see how the different frequency channels will interact in that case. For this exploratory work we use a simple foreground “d0s0” with cosmological parameters set at $r = 0$ and $\beta_b = 0^\circ$. All the prior used in this section have a precision of $\sigma_{\alpha_i} = 1^\circ$. We then draw a random set of biases for each frequency channels. They are drawn from a Gaussian distribution centred at 0° with a standard deviation of 1° following the prior precision. The resulting bias array yields:

$$\Delta\alpha_i = [0.28^\circ, -0.78^\circ, 0.13^\circ, 0.30^\circ, 1.46^\circ, 0.09^\circ] \quad (36)$$

In that context, we explore three cases. First, only one prior on the 93 GHz channel, which is biased by 0.13° following Eq. 36. A second case with priors on all channels, where they are all biased by 0.13° . And the third case with priors on all channels, and all biased by different amounts given by Eq. 36. The central values of the input priors for the three cases are summarised in Tab. V.

The results of the generalised ensemble averaged spectral likelihood sampling for the three cases are displayed in Tab. VI which shows the resulting biases on estimated parameters. In the first case the estimations of the miscalibration angles seem to follow the biased priors and all

	1 biased prior	6 equally biased priors	6 differently biased priors
$\Delta\alpha_{27} [^\circ]$	0.13	0.13	0.24
$\Delta\alpha_{39} [^\circ]$	0.13	0.13	0.24
$\Delta\alpha_{93} [^\circ]$	0.13	0.13	0.25
$\Delta\alpha_{145} [^\circ]$	0.13	0.13	0.25
$\Delta\alpha_{225} [^\circ]$	0.13	0.13	0.25
$\Delta\alpha_{280} [^\circ]$	0.13	0.13	0.25
$\Delta\beta_d$	0.00	0.00	0.00
$\Delta\beta_s$	0.00	0.00	0.00
Δr	0.00	0.00	0.00
$\Delta\beta_b [^\circ]$	-0.13	-0.13	-0.25

TABLE VI. Resulting bias on the estimation of instrumental parameters, spectral indices and cosmological parameters in the 3 biased cases studied here.

polarisation angles have an overall bias of $\Delta\alpha = 0.13^\circ$. Indeed with only one prior all miscalibration angles are estimated *relative* to the channel with a prior. So a biased prior leads to an overall bias.

In the next step of the analysis, the cosmological likelihood, the error is transferred to the estimation of β_b leading to a bias of -0.13° (see Tab. VI). Neither the spectral indices nor r are affected by the bias. Indeed as we mentioned already, since r and β_b are estimated jointly, the method is similar to self-calibration but is performed on a foreground-cleaned and hopefully miscalibration-corrected signal. But even in the case where miscalibration is not well corrected for — as it is the case here — it does not bias the estimation of r .

In the second case with 6 priors and a 0.13° bias on each of them, the estimation of the miscalibration angles are biased by the same value as seen in Tab. VI. This is then biasing β_b as well by -0.13° . Finally in the case where all biases are different we see in the table that all miscalibration angles estimations are biased with the *same* value, 0.25° . It corresponds to the average of all biases values from Eq. 36. So in a sense the less biased channels “help” channels with bigger bias get toward the centre, true value (albeit the other point of view where channels with large bias pull lower biased channels away from the true value is of course equivalent as there is no weighing between channels). This observation can be of interest while analysing data or designing experiments. Since priors on all channels are not essential to restrict β_b , as demonstrated in paragraph V A 1, calibration on one specific channel may be omitted in order to optimise the resulting β_b if it appears to be prone to a particularly large systematic impact that might cause biases. Finally the bias on miscalibration angles is carried to β_b leading to a -0.25° bias (see Tab. VI) and r is again not affected.

VI. CONCLUSION

We propose and apply to simulations a novel method able to perform component separation in the presence of galactic foregrounds and that includes systematic effect correction, with the use of calibration priors. We demonstrate the method on cosmological parameters estimation and forecast its performance on a typical future ground based multi-frequency CMB experiments. To do so we used likelihoods that are semi-analytically averaged over CMB and noise realisations. The results therefore give us the most likely value for the considered parameters estimation as well as their dispersion.

This work is a generalisation of the pixel-based parametric component separation method introduced in [38, 40]. To account for instrumental effects we added the instrumental response matrix \mathbf{X} to the formalism. We also added calibration priors and accounted for their statistical effect all the way to cosmological parameters. The novel method estimating systematic effects with priors simultaneously as performing the component separation in the generalised spectral likelihood allows for prior information to be statistically robustly shared between channels through the stiff scaling laws used in the definition of the mixing matrix \mathbf{A} . The foreground and systematic model is not required to match the real data, however any mismatch would induce a foreground and CMB leakage that will potentially bias cosmological parameters. We tested our method against more complex foregrounds to assess this effect.

We applied this formalism to the specific case of the estimation of r and β_b in the presence of complex foregrounds and non-zero polarisation angles using calibration priors.

We used the Simons Observatory Small Aperture Telescopes characteristics for the forecasting results, and we averaged quantities over CMB and noise realisations. We showed that a prior on only one polarisation angle is enough to fit for all others thanks to the sharing of information from one channel to the other via the mixing matrix, while still being able to estimate accurately foreground spectral indices and therefore to perform component separation. We showed as well that adding multiple calibration priors with the same precision but on different frequency channels allows for an overall better constraint on all polarisation angles. For 1 prior with precision $\sigma_{\alpha_{93}} = 0.1^\circ$ on the 93 GHz channel the best achievable precision on polarisation angle is $\sigma(\alpha_{93}) = 0.099^\circ$, reached on the 93 GHz channel and therefore completely limited by the calibration (within the accuracy provided by the sampling).

Whereas with priors of the same precision on all 6 polarisation angles the best precision becomes $\sigma(\alpha_{225}) = 0.049^\circ$. The estimation of the foreground indices are in agreement with the SO SAT forecast with **FGBuster** [9]. Complex foregrounds do not seem to significantly affect the estimation of polarisation angles however the small sky and frequency coverage of the SATs limits the impact of complex foregrounds with

respect to simpler ones.

After estimating spectral and instrumental parameters we estimate cosmological parameters using maps that are foreground cleaned and systematic effect corrected. We explore the r and β_b parameter space to understand any possible degeneracies between the parameters that could arise from the generalised component separation method of the first step, in particular when complex foregrounds are involved and leak in the cleaned CMB maps. For simple foregrounds matching with the mixing matrix model we show that we are able to accurately measure both r and β_b with $r = 0.0002^{+0.0015}_{-0.0018}$ in agreement with [9]. We get a precision on the birefringence angle of $\sigma(\beta_b) = 0.11^\circ$ for 1 prior on 93 GHz with $\sigma_{\alpha_{93}} = 0.1^\circ$ and $\sigma(\beta_b) = 0.07^\circ$ for a prior on all channels. As for the estimation of polarisation angles in the first step we show that accumulating the calibration campaigns on multiple frequencies has an impact on the final estimation of β_b and may be more efficient than trying to reach a better calibration precision on only one channel. Of course having multiple calibrations of the best possible precision is the most desirable scenario, also up to a certain point only as we showed in Fig. 6 that once a $\mathcal{O}(0.1 \text{ deg})$ prior precision is reached, $\sigma(\beta_b)$ starts being limited by the instrumental noise and by the sky coverage. The exact threshold depends on the experiment but also on the number of prior used, the more priors the higher the threshold is reached. In the presence of complex foregrounds that are unmodeled in the mixing matrix, the forecasts are still robust albeit biased. With “d1s1”, r is the most biased parameter with $r = 0.0016^{+0.0016}_{-0.0018}$ but is still 1- σ compatible with the true value $r = 0$. For the birefringence no detectable bias is seen, even with a much more complex foreground model such as “d7s3” we only *see* a bias more than an order of magnitude below the 1- σ level. The relatively small impact of complex foreground must be put into perspective since the small sky fraction observed by the SAT ($f_{sky} = 0.1$), as well as the relatively small frequency coverage, limits the effect of the spatial variation of spectral indices. Having a larger sky patch while lowering the precision plateau on β_b accessible to the experiments might also imply a larger bias induced by spectral indices spatial variability.

The developed method is able to set constraints on r and β_b in the presence of miscalibration polarisation angles and complex foregrounds in the context of the Simons Observatory without the need of assuming anything about galactic foregrounds that is not already needed in the usual parametric component separation method. However some calibration priors will be needed. We can use this formalism to help guide future calibration or missions requirements, such as the precision of calibration priors and their number, or even the noise level and sky coverage. We also tested how biased priors impact the results of the method. The overall bias on β_b seems to come from the average of biases on all channels.

This could be insightful for future calibration missions as in some cases we might have to choose between the statistical improvement that adding a prior offers and the possible systematic bias that it could induce.

In any case the estimation of r is not biased by the angles involved due to the simultaneous estimation of both r and an absolute angle *after* component separation and after constraining the relative angles between other channels thanks to frequency scalings assumed for foreground signals. The method therefore acts as an efficient self-calibration. The absolute angle estimated jointly with r can then be interpreted as the isotropic birefringence angle provided additional knowledge from priors as we discussed. This relaxation of the requirements on polarisation angle calibration on several channels in the context of r estimation could lead to these extra information being used to better understand other systematic effects and demonstrate the robustness of the experiment. Furthermore this work can be applied to more systematic effects such as the ones induced by rotating half-wave plates, which will be installed on the SO SATs or LiteBIRD; bandpasses should also be taken into account. Both effects have been investigated in a similar framework in Vergès *et al.* [39], but not in the context of birefringence or total polarisation angles of the telescopes. Monelli *et al.* [55] recently explored the effect of HWP non-idealities on birefringence estimation albeit in a simple single frequency case in the absence of foregrounds.

They show that neglecting HWP non-idealities in the map-making induces polarisation angle miscalibrations, and that proper HWP calibration is crucial for accurate cosmic birefringence measurements. Many other effects might also have an impact and need to be investigated such as polarisation efficiency, far sidelobes, T-to-P leakage etc. Finally, we focused on the case of the Simons Observatory but this method can be easily applied to many other experiments, either ground-based, such as CMB-S4 [56], or space-borne, such as LiteBIRD [10].

ACKNOWLEDGEMENT

We thank Clara Vergès, Clément Leloup, Hamza El Bouhargani, Magdy Morshed, Arianna Rizzieri and Simon Biquard for useful discussions. This research used resources of the National Energy Research Scientific Computing Center (NERSC), a U.S. Department of Energy Office of Science User Facility located at Lawrence Berkeley National Laboratory. The authors acknowledge support of the French National Research Agency (Agence National de Recherche) grant, ANR BxB (ANR-17-CE31-0022) and B3DCMB (ANR-17-CE23-0002). Some of the results in this paper have been derived using the `healpy`, `numpy` and `PySM` packages. Some of the figures in this article have been created using `GetDist`.

-
- [1] S. M. Carroll, G. B. Field, and R. Jackiw, Limits on a Lorentz- and parity-violating modification of electrodynamics, *Physical Review D* **41**, 1231 (1990).
 - [2] S. M. Carroll, Quintessence and the rest of the world: Suppressing long-range interactions, *Physical Review Letters* **81**, 3067 (1998).
 - [3] F. Finelli and M. Galaverni, Rotation of linear polarization plane and circular polarization from cosmological pseudoscalar fields, *Physical Review D* **79**, 10.1103/physrevd.79.063002 (2009).
 - [4] M. A. Fedderke, P. W. Graham, and S. Rajendran, Axion dark matter detection with CMB polarization, *Physical Review D* **100**, 1 (2019), arXiv:1903.02666.
 - [5] M. aki Watanabe, S. Kanno, and J. Soda, Imprints of the anisotropic inflation on the cosmic microwave background, *Monthly Notices of the Royal Astronomical Society: Letters* **412**, L83 (2011).
 - [6] A. Lue, L. Wang, and M. Kamionkowski, Cosmological signature of new parity-violating interactions, *Physical Review Letters* **83**, 1506 (1999).
 - [7] S. Saito, K. Ichiki, and A. Taruya, Probing polarization states of primordial gravitational waves with cosmic microwave background anisotropies, *Journal of Cosmology and Astroparticle Physics* **2007** (09), 002.
 - [8] M. H. Abitbol, D. Alonso, S. M. Simon, J. Lashner, K. T. Crowley, A. M. Ali, S. Azzoni, C. Baccigalupi, D. Barron, M. L. Brown, E. Calabrese, J. Carron, Y. Chinone, J. Chluba, G. Coppi, K. D. Crowley, M. Devlin, J. Dunkley, J. Errard, V. Fanfani, N. Galitzki, M. Gerbino, J. C. Hill, B. R. Johnson, B. Jost, B. Keating, N. Krachmalnicoff, A. Kusaka, A. T. Lee, T. Louis, M. S. Madhavacheril, H. McCarrick, J. McMahon, P. D. Meerburg, F. Nati, H. Nishino, L. A. Page, D. Poletti, G. Puglisi, M. J. Randall, A. Rotti, J. Spisak, A. Suzuki, G. P. Teply, C. Vergès, E. J. Wollack, Z. Xu, and M. Zannoni, The simons observatory: gain, bandpass and polarization-angle calibration requirements for b-mode searches, *Journal of Cosmology and Astroparticle Physics* **2021** (05), 032.
 - [9] P. Ade, J. Aguirre, Z. Ahmed, S. Aiola, A. Ali, D. Alonso, M. A. Alvarez, K. Arnold, P. Ashton, J. Austermann, H. Awan, C. Baccigalupi, T. Baidon, D. Barron, N. Battaglia, R. Battye, E. Baxter, A. Bazarko, J. A. Beall, R. Bean, D. Beck, S. Beckman, B. Beringue, F. Bianchini, S. Boada, D. Boettger, J. R. Bond, J. Borrill, M. L. Brown, S. M. Bruno, S. Bryan, E. Calabrese, V. Calafut, P. Calisse, J. Carron, A. Challinor, G. Cheshire, Y. Chinone, J. Chluba, H.-M. S. Cho, S. Choi, G. Coppi, N. F. Cothard, K. Coughlin, D. Crichton, K. D. Crowley, K. T. Crowley, A. Cukierman, J. M. D'Ewart, R. Dünner, T. de Haan, M. Devlin, S. Dicker, J. Didier, M. Dobbs, B. Dober, C. J. Duell, S. Duff, A. Duivenvoorden, J. Dunkley, J. Dusatko, J. Errard, G. Fabbian, S. Feeney, S. Ferraro, P. Fluxà, K. Freese, J. C. Frisch, A. Frolov, G. Fuller, B. Fuzia, N. Galitzki, P. A. Gallardo, J. T. G. Gherzi, J. Gao, E. Gawiser, M. Gerbino, V. Gluscevic, N. Goeckner-Wald, J. Golec, S. Gordon, M. Gralla, D. Green, A. Grigorian, J. Groh, C. Groppe, Y. Guan, J. E. Gudmunds-

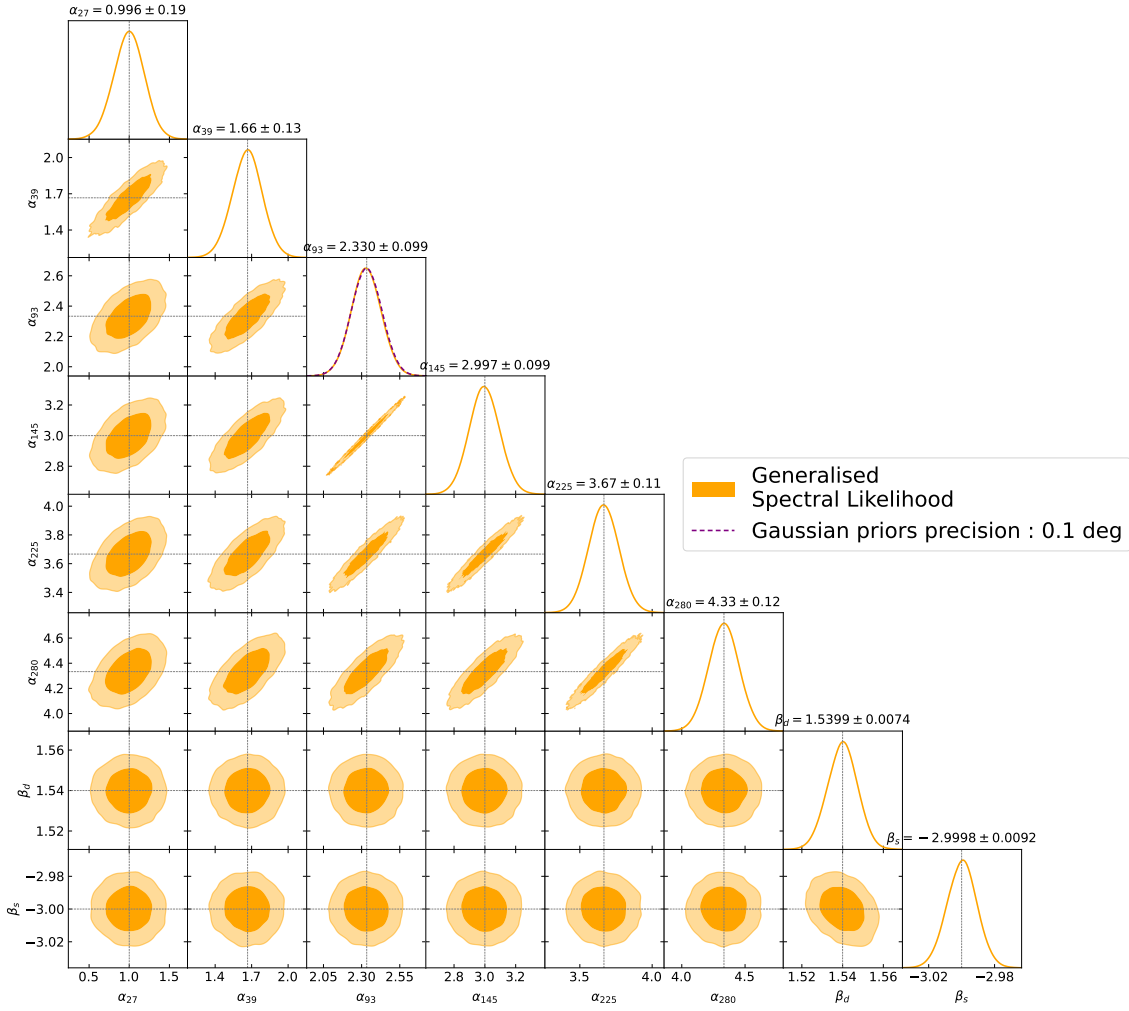


FIG. 7. Results of the generalised spectral likelihood with “d0s0” input foregrounds model. Only one prior on the 93 GHz channel with a precision of $\sigma_{\alpha_{93}} = 0.1^\circ$. The dashed purple lines correspond to the Gaussian priors. The orange contours correspond to the sampling of generalised spectral likelihood. The grey dotted lines corresponds to the input values.

son, D. Han, P. Hargrave, M. Hasegawa, M. Hasselfield, M. Hattori, V. Haynes, M. Hazumi, Y. He, E. Healy, S. W. Henderson, C. Hervias-Caimapo, C. A. Hill, J. C. Hill, G. Hilton, M. Hilton, A. D. Hincks, G. Hinshaw, R. Hložek, S. Ho, S.-P. P. Ho, L. Howe, Z. Huang, J. Hubmayr, K. Hufferberger, J. P. Hughes, A. Ijjas, M. Ikape, K. Irwin, A. H. Jaffe, B. Jain, O. Jeong, D. Kaneko, E. D. Karpel, N. Katayama, B. Keating, S. S. Kerasovskiy, R. Keskitalo, T. Kisner, K. Kiuchi, J. Klein, K. Knowles, B. Koopman, A. Kosowsky, N. Krachmalnicoff, S. E. Kuenstner, C.-L. Kuo, A. Kusaka, J. Lashner, A. Lee, E. Lee, D. Leon, J. S.-Y. Leung, A. Lewis, Y. Li, Z. Li, M. Limon, E. Linder, C. Lopez-Caraballo, T. Louis, L. Lowry, M. Lungu, M. Madhavacheril, D. Mak, F. Maldonado, H. Mani, B. Mates, F. Matsuda, L. Maurin, P. Mauskopf, A. May, N. McCallum, C. McKenney, J. McMahon, P. D. Meerburg, J. Meyers, A. Miller, M. Mirmelstein, K. Moodley, M. Munchmeyer, C. Munson, S. Naess, F. Nati, M. Navaroli, L. Newburgh, H. N. Nguyen, M. Niemack, H. Nishino, J. Orlowski-Scherer, L. Page, B. Partridge, J. Peloton, F. Perrotta, L. Pic-

cirillo, G. Pisano, D. Poletti, R. Puddu, G. Puglisi, C. Raum, C. L. Reichardt, M. Remazeilles, Y. Rephaeli, D. Riechers, F. Rojas, A. Roy, S. Sadeh, Y. Sakurai, M. Salatino, M. S. Rao, E. Schaen, M. Schmittfull, N. Sehgal, J. Seibert, U. Seljak, B. Sherwin, M. Shimon, C. Sierra, J. Sievers, P. Sikhosana, M. Silva-Feaver, S. M. Simon, A. Sinclair, P. Siritanasak, K. Smith, S. R. Smith, D. Spergel, S. T. Staggs, G. Stein, J. R. Stevens, R. Stompor, A. Suzuki, O. Tajima, S. Takakura, G. Teply, D. B. Thomas, B. Thorne, R. Thornton, H. Trac, C. Tsai, C. Tucker, J. Ullom, S. Vagnozzi, A. van Engelen, J. V. Lanen, D. D. V. Winkle, E. M. Vavagiakis, C. Vergès, M. Vissers, K. Wagoner, S. Walker, J. Ward, B. Westbrook, N. Whitehorn, J. Williams, J. Williams, E. J. Wolack, Z. Xu, B. Yu, C. Yu, F. Zago, H. Zhang, and N. Z. and, The simons observatory: science goals and forecasts, *Journal of Cosmology and Astroparticle Physics* **2019** (02), 056.

- [10] LiteBIRD Collaboration, E. Allys, K. Arnold, J. Aumont, R. Aurlien, S. Azzoni, C. Baccigalupi, A. J. Bandy, R. Banerji, R. B. Barreiro, N. Bartolo, L. Bautista,

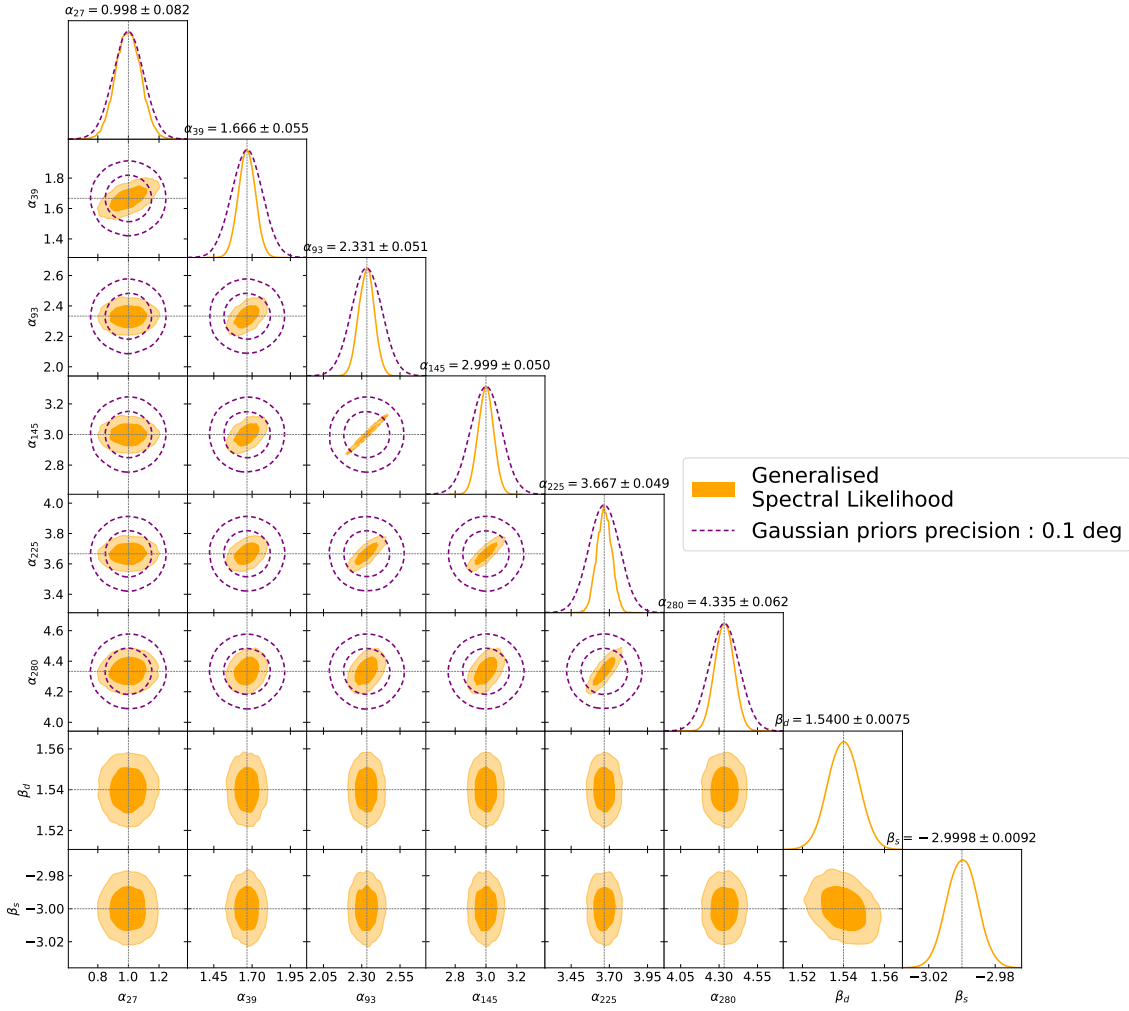


FIG. 8. Results of the generalised spectral likelihood with “d0s0” as input foregrounds model. Priors on all 6 polarisation angles with a precision of $\sigma_{\alpha_i} = 0.1^\circ$. The dashed purple lines correspond to the Gaussian priors. The orange contours correspond to the sampling of generalised spectral likelihood. The grey dotted lines corresponds to the input values.

D. Beck, S. Beckman, M. Bersanelli, F. Boulanger, M. Brilenkov, M. Bucher, E. Calabrese, P. Campeti, A. Carones, F. J. Casas, A. Catalano, V. Chan, K. Cheung, Y. Chinone, S. E. Clark, F. Columbro, G. D’Alessandro, P. de Bernardis, T. de Haan, E. de la Hoz, M. De Petris, S. Della Torre, P. Diego-Palazuelos, T. Dotani, J. M. Duval, T. Elleflot, H. K. Eriksen, J. Errard, T. Essinger-Hileman, F. Finelli, R. Flauger, C. Franceschet, U. Fuskeland, M. Galloway, K. Ganga, M. Gerbino, M. Gervasi, R. T. Génova-Santos, T. Ghigna, S. Giardiello, E. Gjerløw, J. Grain, F. Grupp, A. Gruppuso, J. E. Gudmundsson, N. W. Halverson, P. Hargrave, T. Hasebe, M. Hasegawa, M. Hazumi, S. Henrot-Versillé, B. Hensley, L. T. Hergt, D. Herman, E. Hivon, R. A. Hlozek, A. L. Hornsby, Y. Hoshino, J. Hubmayr, K. Ichiki, T. Iida, H. Imada, H. Ishino, G. Jaehnig, N. Katayama, A. Kato, R. Keskitalo, T. Kisner, Y. Kobayashi, A. Kogut, K. Kohri, E. Komatsu, K. Komatsu, K. Konishi, N. Krachmalnicoff, C. L. Kuo, L. Lamagna, M. Lattanzi, A. T. Lee, C. Leloup, F. Levrier, E. Linder, G. Luzzi, J. Macias-

Perez, B. Maffei, D. Maino, S. Mandelli, E. Martínez-González, S. Masi, M. Massa, S. Matarrese, F. T. Matsuda, T. Matsumura, L. Mele, M. Migliaccio, Y. Minami, A. Moggi, J. Montgomery, L. Montier, G. Morgante, B. Mot, Y. Nagano, T. Nagasaki, R. Nagata, R. Nakano, T. Namikawa, F. Nati, P. Natoli, S. Nerval, F. Noviello, K. Odagiri, S. Oguri, H. Ohsaki, L. Pagano, A. Paiella, D. Paoletti, A. Passerini, G. Patanchon, F. Piacentini, M. Piat, G. Polenta, D. Poletti, T. Prouvé, G. Puglisi, D. Rambaudo, C. Raum, S. Realini, M. Reinecke, M. Remazeilles, A. Ritacco, G. Roudil, J. A. Rubino-Martin, M. Russell, H. Sakurai, Y. Sakurai, M. Sasaki, D. Scott, Y. Sekimoto, K. Shinozaki, M. Shiraishi, P. Shirron, G. Signorelli, F. Spinella, S. Stever, R. Stompor, S. Sugiyama, R. M. Sullivan, A. Suzuki, T. L. Svalheim, E. Switzer, R. Takaku, H. Takakura, Y. Takase, A. Tartari, Y. Terao, J. Thermeau, H. Thommesen, K. L. Thompson, M. Tomasi, M. Tominaga, M. Tristram, M. Tsuji, M. Tsujimoto, L. Vacher, P. Vielva, N. Vittorio, W. Wang, K. Watanuki, I. K. Wehus, J. Weller, B. Westbrook, J. Wilms, E. J. Wollack, J. Yumoto, and M. Zan-

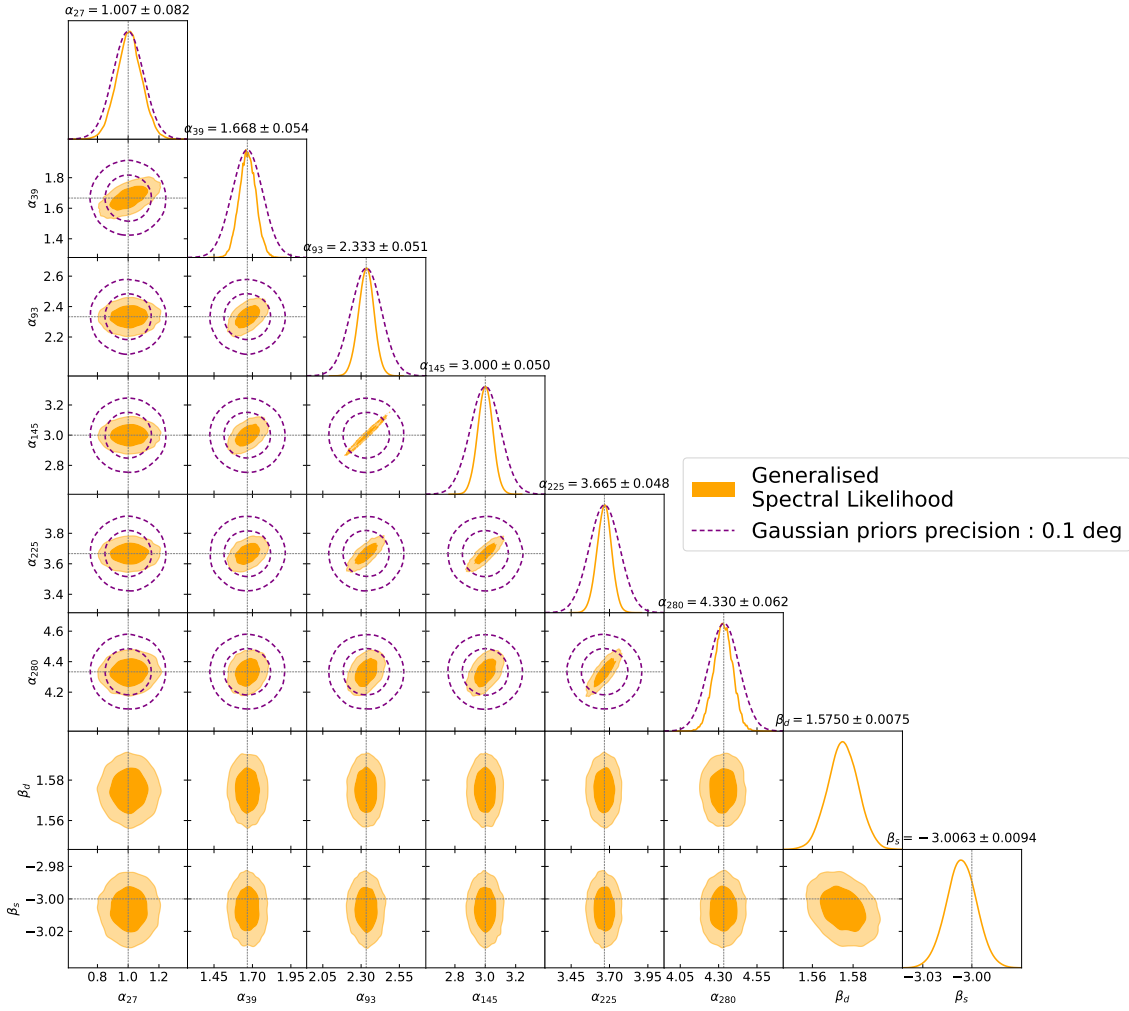


FIG. 9. Results of the generalised spectral likelihood with **s1d1** as input foregrounds model. Priors on all 6 polarisation angles with a precision of $\sigma_{\alpha_i} = 0.1^\circ$. The dashed purple lines correspond to the Gaussian priors. The orange contours correspond to the sampling of generalised spectral likelihood. The grey dotted lines corresponds to the input values.

noni, Probing cosmic inflation with the litebird cosmic microwave background polarization survey (2022).

- [11] P. Vielva, E. Martí nez-González, F. Casas, T. Matsumura, S. Henrot-Versillé, E. Komatsu, J. Aumont, R. Aurlen, C. Baccigalupi, A. Banday, R. Barreiro, N. Bartolo, E. Calabrese, K. Cheung, F. Columbro, A. Coppolecchia, P. de Bernardis, T. de Haan, E. de la Hoz, M. D. Petris, S. D. Torre, P. Diego-Palazuelos, H. Eriksen, J. Errard, F. Finelli, C. Franceschet, U. Fuskeland, M. Galloway, K. Ganga, M. Gervasi, R. Génova-Santos, T. Ghigna, E. Gjerløw, A. Gruppuso, M. Hazumi, D. Herranz, E. Hivon, K. Kohri, L. Lamagna, C. Leloup, J. Macias-Perez, S. Masi, F. Matsuda, G. Morgante, R. Nakano, F. Nati, P. Natoli, S. Nerval, K. Odagiri, S. Oguri, L. Pagano, A. Paiella, D. Paoletti, F. Piacentini, G. Polenta, G. Puglisi, M. Remazeilles, A. Ritacco, J. Rubino-Martin, D. Scott, Y. Sekimoto, M. Shiraishi, G. Signorelli, H. Takakura, A. Tartari, K. Thompson, M. Tristram, L. Vacher, N. Vittorio, I. Wehus, and M. Zannoni, Polarization angle requirements for CMB b-mode experiments. application to the LiteBIRD satellite,

Journal of Cosmology and Astroparticle Physics **2022** (04), 029.

- [12] P. A. R. Ade, Z. Ahmed, M. Amiri, D. Barkats, R. Basu Thakur, C. A. Bischoff, J. J. Bock, H. Boenish, E. Bullock, V. Buza, J. R. Cheshire, J. Connors, J. Cornelison, M. Crumrine, A. Cukierman, M. Dierickx, L. Duband, S. Fatigoni, J. P. Filippini, S. Fliescher, N. Goeckner-Wald, J. Grayson, G. Hall, M. Halpern, S. Harrison, S. Henderson, S. R. Hildebrandt, G. C. Hilton, J. Hubmayr, H. Hui, K. D. Irwin, J. Kang, K. S. Karkare, E. Karpel, B. G. Keating, S. Kefeli, S. A. Kernasovskiy, J. M. Kovac, C. L. Kuo, K. Lau, E. M. Leitch, K. G. Megerian, L. Monceli, T. Namikawa, C. B. Netterfield, H. T. Nguyen, R. O'Brient, R. W. Ogburn, S. Palladino, T. Prouve, C. Pryke, B. Racine, C. D. Reintsema, S. Richter, A. Schillaci, B. L. Schmitt, R. Schwarz, C. D. Sheehy, A. Soliman, T. S. Germaine, B. Steinbach, R. V. Sudiwala, G. Teply, K. L. Thompson, J. E. Tolan, C. Tucker, A. D. Turner, C. Umiltà, A. G. Viereg, A. Wandui, A. C. Weber, D. V. Wiebe, J. Willmert, C. L. Wong, W. L. K. Wu, H. Yang, K. W. Yoon, E. Young,

- C. Yu, L. Zeng, and C. Zhang (BICEP/Keck Collaboration), BICEP/keck xii: Constraints on axionlike polarization oscillations in the cosmic microwave background, *Phys. Rev. D* **103**, 042002 (2021).
- [13] P. A. R. Ade, Z. Ahmed, M. Amiri, D. Barkats, R. Basu Thakur, C. A. Bischoff, D. Beck, J. J. Bock, H. Boenish, E. Bullock, V. Buza, J. R. Cheshire, J. Connors, J. Cornelison, M. Crumrine, A. Cukierman, E. V. Denison, M. Dierickx, L. Duband, M. Eiben, S. Fatigoni, J. P. Filippini, S. Fliescher, N. Goeckner-Wald, D. C. Goldfinger, J. Grayson, P. Grimes, G. Hall, G. Halal, M. Halpern, E. Hand, S. Harrison, S. Henderson, S. R. Hildebrandt, G. C. Hilton, J. Hubmayr, H. Hui, K. D. Irwin, J. Kang, K. S. Karkare, E. Karpel, S. Kefeli, S. A. Kernasovskiy, J. M. Kovac, C. L. Kuo, K. Lau, E. M. Leitch, A. Lennox, K. G. Megerian, L. Minutolo, L. Monceli, Y. Nakato, T. Namikawa, H. T. Nguyen, R. O'Brient, R. W. Ogburn, S. Paladino, T. Prouve, C. Pryke, B. Racine, C. D. Reintsema, S. Richter, A. Schillaci, R. Schwarz, B. L. Schmitt, C. D. Sheehy, A. Soliman, T. S. Germaine, B. Steinbach, R. V. Sudiwala, G. P. Teply, K. L. Thompson, J. E. Tolan, C. Tucker, A. D. Turner, C. Umiltà, C. Vergès, A. G. Vieregg, A. Wandui, A. C. Weber, D. V. Wiebe, J. Willmert, C. L. Wong, W. L. K. Wu, H. Yang, K. W. Yoon, E. Young, C. Yu, L. Zeng, C. Zhang, and S. Zhang (BICEP/Keck Collaboration), Bicep/keck xiv: Improved constraints on axionlike polarization oscillations in the cosmic microwave background, *Phys. Rev. D* **105**, 022006 (2022).
- [14] K. R. Ferguson *et al.* (SPT-3G), Searching for axionlike time-dependent cosmic birefringence with SPT-3G, (2022), arXiv:2203.16567 [astro-ph.CO].
- [15] B. G. Keating, M. Shimon, and A. P. S. Yadav, SELF-CALIBRATION OF COSMIC MICROWAVE BACKGROUND POLARIZATION EXPERIMENTS, *The Astrophysical Journal* **762**, L23 (2012).
- [16] Y. Minami, H. Ochi, K. Ichiki, N. Katayama, E. Komatsu, and T. Matsumura, Simultaneous determination of the cosmic birefringence and miscalibrated polarisation angles from cmb experiments (2019).
- [17] P. Diego-Palazuelos, J. Eskilt, Y. Minami, M. Tristram, R. Sullivan, A. Banday, R. Barreiro, H. Eriksen, K. Górski, R. Keskitalo, E. Komatsu, E. Martínez-González, D. Scott, P. Vielva, and I. Wehus, Cosmic birefringence from the planck data release 4, *Physical Review Letters* **128**, 10.1103/physrevlett.128.091302 (2022).
- [18] Y. Minami and E. Komatsu, New extraction of the cosmic birefringence from the planck 2018 polarization data, *Physical Review Letters* **125**, 10.1103/physrevlett.125.221301 (2020).
- [19] S. E. Clark, C.-G. Kim, J. C. Hill, and B. S. Hensley, The origin of parity violation in polarized dust emission and implications for cosmic birefringence, *The Astrophysical Journal* **919**, 53 (2021).
- [20] K. M. Huffmanberger, A. Rotti, and D. C. Collins, The power spectra of polarized, dusty filaments, *The Astrophysical Journal* **899**, 31 (2020).
- [21] Y. Akrami, M. Ashdown, J. Aumont, C. Baccigalupi, M. Ballardini, A. J. Banday, R. B. Barreiro, N. Bartolo, S. Basak, K. Benabed, M. Bersanelli, P. Bielewicz, J. R. Bond, J. Borrill, F. R. Bouchet, F. Boulanger, M. Bucher, C. Burigana, E. Calabrese, J. F. Cardoso, J. Carron, B. Casaponsa, A. Challinor, L. P. Colombo, C. Combet, B. P. Crill, F. Cuttaia, P. De Bernardis, A. De Rosa, G. De Zotti, J. Delabrouille, J. M. Delouis, E. Di Valentino, C. Dickinson, J. M. Diego, S. Donzelli, O. Doré, A. Ducout, X. Dupac, G. Efstathiou, F. Elsner, T. A. Enßlin, H. K. Eriksen, E. Falgarone, R. Fernandez-Cobos, F. Finelli, F. Forastieri, M. Frailis, A. A. Fraisse, E. Franceschi, A. Frolov, S. Galeotta, S. Galli, K. Ganga, R. T. Génova-Santos, M. Gerbino, T. Ghosh, J. González-Nuevo, K. M. Górski, S. Gratton, A. Gruppuso, J. E. Gudmundsson, W. Handley, F. K. Hansen, G. Helou, D. Herranz, S. R. Hildebrandt, Z. Huang, A. H. Jaffe, A. Karakci, E. Keihänen, R. Keskitalo, K. Kiiveri, J. Kim, T. S. Kisner, N. Krachmalnicoff, M. Kunz, H. Kurki-Suonio, G. Lagache, J. M. Lamarre, A. Lasenby, M. Lattanzi, C. R. Lawrence, M. Le Jeune, F. Levrier, M. Liguori, P. B. Lilje, V. Lindholm, M. López-Caniego, P. M. Lubin, Y. Z. Ma, J. F. Macías-Pérez, G. Maggio, D. Maino, N. Mandolesi, A. Mangilli, A. Marcos-Caballero, M. Maris, P. G. Martin, E. Martínez-González, S. Matarrese, N. Mauri, J. D. McEwen, P. R. Meinhold, A. Melchiorri, A. Mennella, M. Migliaccio, M. A. Miville-Deschênes, D. Molinari, A. Moneti, L. Montier, G. Morgante, P. Natoli, F. Oppizzi, L. Pagano, D. Paoletti, B. Partridge, M. Peel, V. Pettorino, F. Piacentini, G. Polenta, J. L. Puget, J. P. Rachen, M. Reinecke, M. Remazeilles, A. Renzi, G. Rocha, G. Roudier, J. A. Rubiño-Martín, B. Ruiz-Granados, L. Salvati, M. Sandri, M. Savelainen, D. Scott, D. S. Seljebotn, C. Sirignano, L. D. Spencer, A. S. Suur-Uski, J. A. Tauber, D. Tavagnacco, M. Tenti, H. Thommesen, L. Toffolatti, M. Tomasi, T. Trombetti, J. Valiviita, B. Van Tent, P. Vielva, F. Villa, N. Vittorio, B. D. Wandelt, I. K. Wehus, A. Zacchei, and A. Zonca, Planck 2018 results: IV. Diffuse component separation, *Astronomy and Astrophysics* **641**, 1 (2020), arXiv:1807.06208.
- [22] J. R. Eskilt and E. Komatsu, Improved constraints on cosmic birefringence from the wmap and planck cosmic microwave background polarization data (2022).
- [23] J. R. Eskilt, Frequency-dependent constraints on cosmic birefringence from the LFI and HFI planck data release 4, *Astronomy & Astrophysics* **662**, A10 (2022).
- [24] B. D. Sherwin and T. Namikawa, Cosmic birefringence tomography and calibration-independence with reionization signals in the cmb 10.48550/ARXIV.2108.09287 (2021).
- [25] J. Aumont, J. F. Macías-Pérez, A. Ritacco, N. Ponthieu, and A. Mangilli, Absolute calibration of the polarisation angle for future CMB b-mode experiments from current and future measurements of the crab nebula, *Astronomy & Astrophysics* **634**, A100 (2020).
- [26] A. Ritacco, J. F. Macías-Pérez, N. Ponthieu, R. Adam, P. Ade, P. André, J. Aumont, A. Beelen, A. Benoît, A. Bideaud, N. Billot, O. Bourrion, A. Bracco, M. Calvo, A. Catalano, G. Coiffard, B. Comis, A. D'Addabbo, M. D. Petris, F.-X. Désert, S. Doyle, J. Goupy, C. Kramer, G. Lagache, S. Leclercq, J.-F. Lestrade, P. Mäuskopf, F. Mayet, A. Maury, A. Monfardini, F. Pajot, E. Pascale, L. Perotto, G. Pisano, M. Rebolo-Iglesias, V. Revéret, L. Rodriguez, C. Romero, H. Rousset, F. Ruppen, K. Schuster, A. Sievers, G. Siringo, C. Thum, S. Triqueneaux, C. Tucker, H. Wiesemeyer, and R. Zylka, NIKA 150 GHz polarization observations of the crab nebula and its spectral energy distribution,

- Astronomy & Astrophysics **616**, A35 (2018).
- [27] S. A. Bryan, G. P. Teply, S. M. Simon, M. Gerbino, A. Ali, Y. Chinone, K. Crowley, G. Fabbian, P. Gallardo, N. Goeckner-Wald, B. Keating, B. Koopman, A. Kusaka, F. Matsuda, P. Mauskopf, J. McMahon, F. Nati, G. Puglisi, C. Reichardt, M. Salatino, Z. Xu, and N. Zhu, Development of calibration strategies for the simons observatory, in *Millimeter, Submillimeter, and Far-Infrared Detectors and Instrumentation for Astronomy IX*, edited by J. Zmuidzinas and J.-R. Gao (SPIE, 2018).
 - [28] F. Nati, M. J. Devlin, M. Gerbino, B. R. Johnson, B. Keating, L. Pagano, and G. Teply, POLO-CALC: A novel method to measure the absolute polarization orientation of the cosmic microwave background, *Journal of Astronomical Instrumentation* **06**, 10.1142/s2251171717400086 (2017).
 - [29] J. W. Fowler, M. D. Niemack, S. R. Dicker, A. M. Aboobaker, P. A. R. Ade, E. S. Battistelli, M. J. Devlin, R. P. Fisher, M. Halpern, P. C. Hargrave, A. D. Hincks, M. Kaul, J. Klein, J. M. Lau, M. Limon, T. A. Marriage, P. D. Mauskopf, L. Page, S. T. Staggs, D. S. Swetz, E. R. Switzer, R. J. Thornton, and C. E. Tucker, Optical design of the atacama cosmology telescope and the millimeter bolometric array camera, *Appl. Opt.* **46**, 3444 (2007).
 - [30] R. J. Thornton, P. A. R. Ade, S. Aiola, F. E. Angilè, M. Amiri, J. A. Beall, D. T. Becker, H.-M. Cho, S. K. Choi, P. Corlies, K. P. Coughlin, R. Datta, M. J. Devlin, S. R. Dicker, R. Dünner, J. W. Fowler, A. E. Fox, P. A. Gallardo, J. Gao, E. Grace, M. Halpern, M. Hasselfield, S. W. Henderson, G. C. Hilton, A. D. Hincks, S. P. Ho, J. Hubmayr, K. D. Irwin, J. Klein, B. Koopman, D. Li, T. Louis, M. Lungu, L. Maurin, J. McMahon, C. D. Munson, S. Naess, F. Nati, L. Newburgh, J. Nibarger, M. D. Niemack, P. Niraula, M. R. Nolta, L. A. Page, C. G. Pappas, A. Schillaci, B. L. Schmitt, N. Sehgal, J. L. Sievers, S. M. Simon, S. T. Staggs, C. Tucker, M. Uehara, J. van Lanen, J. T. Ward, and E. J. Wollack, THE ATACAMA COSMOLOGY TELESCOPE: THE POLARIZATION-SENSITIVE ACTPol INSTRUMENT, *The Astrophysical Journal Supplement Series* **227**, 21 (2016), arXiv:1605.06569.
 - [31] T. Essinger-Hileman, A. Ali, M. Amiri, J. W. Appel, D. Araujo, C. L. Bennett, F. Boone, M. Chan, H.-M. Cho, D. T. Chuss, F. Colazo, E. Crowe, K. Denis, R. Dünner, J. Eimer, D. Gothe, M. Halpern, K. Harrington, G. C. Hilton, G. F. Hinshaw, C. Huang, K. Irwin, G. Jones, J. Karakla, A. J. Kogut, D. Larson, M. Limon, L. Lowry, T. Marriage, N. Mehrle, A. D. Miller, N. Miller, S. H. Moseley, G. Novak, C. Reintsema, K. Rostem, T. Stevenson, D. Towner, K. U-Yen, E. Wagner, D. Watts, E. J. Wollack, Z. Xu, and L. Zeng, CLASS: the cosmology large angular scale surveyor, in *SPIE Proceedings*, edited by W. S. Holland and J. Zmuidzinas (SPIE, 2014).
 - [32] C. L. Bennett, R. S. Hill, G. Hinshaw, M. R. Nolta, N. Odegard, L. Page, D. N. Spergel, J. L. Weiland, E. L. Wright, M. Halpern, N. Jarosik, A. Kogut, M. Limon, S. S. Meyer, G. S. Tucker, and E. Wollack, First-year wilkinson microwave anisotropy probe (wmap) observations: Foreground emission, *The Astrophysical Journal Supplement Series* **148**, 97 (2003).
 - [33] M. Remazeilles, J. Delabrouille, and J.-F. Cardoso, Foreground component separation with generalized internal linear combination, *Monthly Notices of the Royal Astronomical Society* **418**, 467 (2011).
 - [34] J. Delabrouille, J.-F. Cardoso, M. L. Jeune, M. Betoule, G. Fay, and F. Guillaoux, A full sky, low foreground, high resolution CMB map from WMAP, *Astronomy & Astrophysics* **493**, 835 (2008).
 - [35] J.-F. Cardoso, M. Martin, J. Delabrouille, M. Betoule, and G. Patanchon, Component separation with flexible models. application to the separation of astrophysical emissions (2008).
 - [36] H. K. Eriksen, C. Dickinson, C. R. Lawrence, C. Baccigalupi, A. J. Banday, K. M. Gorski, F. K. Hansen, P. B. Lilje, E. Pierpaoli, M. D. Seiffert, K. M. Smith, and K. Vanderlinde, Cosmic microwave background component separation by parameter estimation, *The Astrophysical Journal* **641**, 665 (2006).
 - [37] H. K. Eriksen, J. B. Jewell, C. Dickinson, A. J. Banday, K. M. Górski, and C. R. Lawrence, Joint bayesian component separation and CMB power spectrum estimation, *The Astrophysical Journal* **676**, 10 (2008).
 - [38] R. Stompor, S. Leach, F. Stivoli, and C. Baccigalupi, Maximum likelihood algorithm for parametric component separation in cosmic microwave background experiments, *Monthly Notices of the Royal Astronomical Society* **392**, 216 (2008), <https://academic.oup.com/mnras/article-pdf/392/1/216/3707574/mnras0392-0216.pdf>.
 - [39] C. Vergès, J. Errard, and R. Stompor, Framework for analysis of next generation, polarized cmb data sets in the presence of galactic foregrounds and systematic effects, *Phys. Rev. D* **103**, 063507 (2021).
 - [40] R. Stompor, J. Errard, and D. Poletti, Forecasting performance of cmb experiments in the presence of complex foreground contaminations, *Phys. Rev. D* **94**, 083526 (2016).
 - [41] D. Beck, J. Errard, and R. Stompor, Impact of polarized galactic foreground emission on CMB lensing reconstruction and delensing of b-modes, *Journal of Cosmology and Astroparticle Physics* **2020** (06), 030.
 - [42] LiteBIRD Collaboration, E. Allys, K. Arnold, J. Aumont, R. Aurlien, S. Azzoni, C. Baccigalupi, A. J. Banday, R. Banerji, R. B. Barreiro, N. Bartolo, L. Bautista, D. Beck, S. Beckman, M. Bersanelli, F. Boulanger, M. Brilenkov, M. Bucher, E. Calabrese, P. Campeti, A. Carones, F. J. Casas, A. Catalano, V. Chan, K. Cheung, Y. Chinone, S. E. Clark, F. Columbro, G. D'Alessandro, P. de Bernardis, T. de Haan, E. de la Hoz, M. De Petris, S. Della Torre, P. Diego-Palazuelos, T. Dotani, J. M. Duval, T. Elleflot, H. K. Eriksen, J. Errard, T. Essinger-Hileman, F. Finelli, R. Flauger, C. Franceschet, U. Fuskeland, M. Galloway, K. Ganga, M. Gerbino, M. Gervasi, R. T. Génova-Santos, T. Ghigna, S. Giardiello, E. Gjerløw, J. Grain, F. Grupp, A. Gruppuso, J. E. Gudmundsson, N. W. Halverson, P. Hargrave, T. Hasebe, M. Hasegawa, M. Hazumi, S. Henrot-Versillé, B. Hensley, L. T. Hergt, D. Herman, E. Hivon, R. A. Hlozek, A. L. Hornsby, Y. Hoshino, J. Hubmayr, K. Ichiki, T. Iida, H. Imada, H. Ishino, G. Jaehnig, N. Katayama, A. Kato, R. Kesitalo, T. Kisner, Y. Kobayashi, A. Kogut, K. Kohri, E. Komatsu, K. Komatsu, K. Konishi, N. Krachmalnicoff, C. L. Kuo, L. Lamagna, M. Lattanzi, A. T. Lee, C. Leloup, F. Levrier, E. Linder, G. Luzzi, J. Macias-Perez, B. Maffei, D. Maino, S. Mandelli, E. Martínez-

- González, S. Masi, M. Massa, S. Matarrese, F. T. Matsuda, T. Matsumura, L. Mele, M. Migliaccio, Y. Minami, A. Moggi, J. Montgomery, L. Montier, G. Morgante, B. Mot, Y. Nagano, T. Nagasaki, R. Nagata, R. Nakano, T. Namikawa, F. Nati, P. Natoli, S. Nerval, F. Noviello, K. Odagiri, S. Oguri, H. Ohsaki, L. Pagano, A. Paiella, D. Paoletti, A. Passerini, G. Patanchon, F. Piacentini, M. Piat, G. Polenta, D. Poletti, T. Prouvé, G. Puglisi, D. Rambaud, C. Raum, S. Realini, M. Reinecke, M. Remazeilles, A. Ritacco, G. Roudil, J. A. Rubino-Martin, M. Russell, H. Sakurai, Y. Sakurai, M. Sasaki, D. Scott, Y. Sekimoto, K. Shinozaki, M. Shiraishi, P. Shirron, G. Signorelli, F. Spinella, S. Stever, R. Stompor, S. Sugiyama, R. M. Sullivan, A. Suzuki, T. L. Svalheim, E. Switzer, R. Takaku, H. Takakura, Y. Takase, A. Tartari, Y. Terao, J. Thermeau, H. Thommesen, K. L. Thompson, M. Tomasi, M. Tominaga, M. Tristram, M. Tsuji, M. Tsujimoto, L. Vacher, P. Vielva, N. Vittorio, W. Wang, K. Watanuki, I. K. Wehus, J. Weller, B. Westbrook, J. Wilms, E. J. Wollack, J. Yumoto, and M. Zannoni, Probing cosmic inflation with the lite-bird cosmic microwave background polarization survey 10.48550/ARXIV.2202.02773 (2022).
- [43] J. Errard, M. Remazeilles, J. Aumont, J. Delabrouille, D. Green, S. Hanany, B. S. Hensley, and A. Kogut, Constraints on the Optical Depth to Reionization from Balloon-borne Cosmic Microwave Background Measurements, *Astrophys. J.* **940**, 68 (2022), arXiv:2206.03389 [astro-ph.CO].
- [44] M. Tegmark, A. N. Taylor, and A. F. Heavens, eve Eigenvalue Problems in Cosmology : How should we Tackle Large Data Sets ?, (2008), arXiv:9603021v2 [arXiv:astro-ph].
- [45] A. Zonca, L. Singer, D. Lenz, M. Reinecke, C. Rosset, E. Hivon, and K. Gorski, healpy: equal area pixelization and spherical harmonics transforms for data on the sphere in python, *Journal of Open Source Software* **4**, 1298 (2019).
- [46] K. M. Górski, E. Hivon, A. J. Banday, B. D. Wandelt, F. K. Hansen, M. Reinecke, and M. Bartelmann, HEALPix: A Framework for High-Resolution Discretization and Fast Analysis of Data Distributed on the Sphere, *Astrophys. J.* **622**, 759 (2005), arXiv:astro-ph/0409513.
- [47] N. Aghanim, Y. Akrami, M. Ashdown, J. Aumont, C. Baccigalupi, M. Ballardini, A. J. Banday, R. B. Barreiro, N. Bartolo, S. Basak, R. Battye, K. Benabed, J. P. Bernard, M. Bersanelli, P. Bielewicz, J. J. Bock, J. R. Bond, J. Borrill, F. R. Bouchet, F. Boulanger, M. Bucher, C. Burigana, R. C. Butler, E. Calabrese, J. F. Cardoso, J. Carron, A. Challinor, H. C. Chiang, J. Chluba, L. P. Colombo, C. Combet, D. Contreras, B. P. Crill, F. Cuttaia, P. De Bernardis, G. De Zotti, J. Delabrouille, J. M. Delouis, E. Di Valentino, J. M. Diego, O. Doré, M. Douspis, A. Ducout, X. Dupac, S. Dusini, G. Efstathiou, F. Elsner, T. A. Enßlin, H. K. Eriksen, Y. Fantaye, M. Farhang, J. Fergusson, R. Fernandez-Cobos, F. Finelli, F. Forastieri, M. Frailis, A. A. Fraisse, E. Franceschi, A. Frolov, S. Galeotta, S. Galli, K. Ganga, R. T. Génova-Santos, M. Gerbino, T. Ghosh, J. González-Nuevo, K. M. Górski, S. Gratton, A. Gruppuso, J. E. Gudmundsson, J. Hamann, W. Handley, F. K. Hansen, D. Herranz, S. R. Hildebrandt, E. Hivon, Z. Huang, A. H. Jaffe, W. C. Jones, A. Karakci, E. Keihänen, R. Keskitalo, K. Kiiveri, J. Kim, T. S. Kisner, L. Knox, N. Krachmalnicoff, M. Kunz, H. Kurki-Suonio, G. Lagache, J. M. Lamarre, A. Lasenby, M. Lattanzi, C. R. Lawrence, M. Le Jeune, P. Lemos, J. Lesgourgues, F. Levrier, A. Lewis, M. Liguori, P. B. Lilje, M. Lilley, V. Lindholm, M. López-Caniego, P. M. Lubin, Y. Z. Ma, J. F. Macías-Pérez, G. Maggio, D. Maino, N. Mandolesi, A. Mangilli, A. Marcos-Caballero, M. Maris, P. G. Martin, M. Martinelli, E. Martínez-González, S. Matarrese, N. Mauri, J. D. McEwen, P. R. Meinhold, A. Melchiorri, A. Mennella, M. Migliaccio, M. Millea, S. Mitra, M. A. Miville-Deschênes, D. Molinari, L. Montier, G. Morgante, A. Moss, P. Natoli, H. U. Nørgaard-Nielsen, L. Pagano, D. Paoletti, B. Partridge, G. Patanchon, H. V. Peiris, F. Perrotta, V. Pettorino, F. Piacentini, L. Polastri, G. Polenta, J. L. Puget, J. P. Rachen, M. Reinecke, M. Remazeilles, A. Renzi, G. Rocha, C. Rosset, G. Roudier, J. A. Rubiño-Martín, B. Ruiz-Granados, L. Salvati, M. Sandri, M. Savelainen, D. Scott, E. P. Shellard, C. Sirignano, G. Sirri, L. D. Spencer, R. Sunyaev, A. S. Suur-Uski, J. A. Tauber, D. Tavagnacco, M. Tenti, L. Toffolatti, M. Tomasi, T. Trombetti, L. Valenziano, J. Valiviita, B. Van Tent, L. Vibert, P. Vielva, F. Villa, N. Vittorio, B. D. Wandelt, I. K. Wehus, M. White, S. D. White, A. Zacchei, and A. Zonca, Planck 2018 results: VI. Cosmological parameters, *Astronomy and Astrophysics* **641**, 10.1051/0004-6361/201833910 (2020), arXiv:1807.06209.
- [48] B. Thorne, J. Dunkley, D. Alonso, and S. Næss, The python sky model: software for simulating the galactic microwave sky, *Monthly Notices of the Royal Astronomical Society* **469**, 2821 (2017).
- [49] D. Foreman-Mackey, D. W. Hogg, D. Lang, and J. Goodman, emcee: The mcmc hammer, *Publications of the Astronomical Society of the Pacific* **125**, 306 (2013).
- [50] K. Wolz et al, The Simons Observatory: pipeline comparison and validation for large-scale B-modes, (in prep).
- [51] R. Adam, P. A. Ade, N. Aghanim, M. I. Alves, M. Arnaud, M. Ashdown, J. Aumont, C. Baccigalupi, A. J. Banday, R. B. Barreiro, J. G. Bartlett, N. Bartolo, E. Battaner, K. Benabed, A. Benoît, A. Benoit-Lévy, J. P. Bernard, M. Bersanelli, P. Bielewicz, J. J. Bock, A. Bonaldi, L. Bonavera, J. R. Bond, J. Borrill, F. R. Bouchet, F. Boulanger, M. Bucher, C. Burigana, R. C. Butler, E. Calabrese, J. F. Cardoso, A. Catalano, A. Challinor, A. Chaballu, R. R. Chary, H. C. Chiang, P. R. Christensen, D. L. Clements, S. Colombi, L. P. Colombo, C. Combet, F. Couchot, A. Coulais, B. P. Crill, A. Curto, F. Cuttaia, L. Danese, R. D. Davies, R. J. Davis, P. De Bernardis, A. De Rosa, G. De Zotti, J. Delabrouille, F. X. Désert, C. Dickinson, J. M. Diego, H. Dole, S. Donzelli, O. Doré, M. Douspis, A. Ducout, X. Dupac, G. Efstathiou, F. Elsner, T. A. Enßlin, H. K. Eriksen, E. Falgarone, J. Fergusson, F. Finelli, O. Forni, M. Frailis, A. A. Fraisse, E. Franceschi, A. Frejsel, S. Galeotta, S. Galli, K. Ganga, T. Ghosh, M. Girard, Y. Giraud-Héraud, E. Gjerløw, J. González-Nuevo, K. M. Górski, S. Gratton, A. Gregorio, A. Gruppuso, J. E. Gudmundsson, F. K. Hansen, D. Hanson, D. L. Harrison, G. Helou, S. Henrot-Versillé, C. Hernández-Monteagudo, D. Herranz, S. R. Hildebrandt, E. Hivon, M. Hobson, W. A. Holmes, A. Hornstrup, W. Hovest, K. M. Hufenberger, G. Hurier, A. H. Jaffe, T. R. Jaffe, W. C. Jones, M. Juvela, E. Keihänen, R. Keskitalo,

- T. S. Kisner, R. Kneissl, J. Knoche, M. Kunz, H. Kurki-Suonio, G. Lagache, A. Lähteenmäki, J. M. Lamarre, A. Lasenby, M. Lattanzi, C. R. Lawrence, M. Le Jeune, J. P. Leahy, R. Leonardi, J. Lesgourgues, F. Levrier, M. Liguori, P. B. Lilje, M. Linden-Vørnle, M. López-Caniego, P. M. Lubin, J. F. Macías-Pérez, G. Maggio, D. Maino, N. Mandolesi, A. Mangilli, M. Maris, D. J. Marshall, P. G. Martin, E. Martínez-González, S. Masi, S. Matarrese, P. McGehee, P. R. Meinhold, A. Melchiorri, L. Mendes, A. Mennella, M. Migliaccio, S. Mitra, M. A. Miville-Deschênes, A. Moneti, L. Montier, G. Morgante, D. Mortlock, A. Moss, D. Munshi, J. A. Murphy, P. Naselsky, F. Nati, P. Natoli, C. B. Netterfield, H. U. Nørgaard-Nielsen, F. Noviello, D. Novikov, I. Novikov, E. Orlando, C. A. Oxborrow, F. Paci, L. Pagano, F. Pajot, R. Paladini, D. Paoletti, B. Partridge, F. Pasian, G. Patanchon, T. J. Pearson, O. Perdereau, L. Perotto, F. Perrotta, V. Pettorino, F. Piacentini, M. Piat, E. Pierpaoli, D. Pietrobon, S. Plaszczynski, E. Pointecouteau, G. Polenta, G. W. Pratt, G. Prézeau, S. Prunet, J. L. Puget, J. P. Rachen, W. T. Reach, R. Rebolo, M. Reinecke, M. Remazeilles, C. Renault, A. Renzi, I. Ristorcelli, G. Rocha, C. Rosset, M. Rossetti, G. Roudier, J. A. Rubinó-Martín, B. Rusholme, M. Sandri, D. Santos, M. Savelainen, G. Savini, D. Scott, M. D. Seiffert, E. P. Shellard, L. D. Spencer, V. Stolyarov, R. Stompor, A. W. Strong, R. Sudiwala, R. Sunyaev, D. Sutton, A. S. Suur-Uski, J. F. Sygnet, J. A. Tauber, L. Terenzi, L. Tofolatti, M. Tomasi, M. Tristram, M. Tucci, J. Tuovinen, G. Umana, L. Valenziano, J. Valiviita, F. Van Tent, P. Vielva, F. Villa, L. A. Wade, B. D. Wandelt, I. K. Wehus, A. Wilkinson, D. Yvon, A. Zacchei, and A. Zonca, Planck 2015 results: X. Diffuse component separation: Foreground maps, *Astronomy and Astrophysics* **594**, 1 (2016), arXiv:1502.01588.
- [52] B. T. Draine and B. Hensley, MAGNETIC NANOPARTICLES IN THE INTERSTELLAR MEDIUM: EMISSION SPECTRUM AND POLARIZATION, *The Astrophysical Journal* **765**, 159 (2013).
- [53] B. Hensley, *On the nature of interstellar grains*, Ph.D. thesis (2015).
- [54] N. Aghanim *et al.* (Planck), Planck 2018 results. VI. Cosmological parameters, *Astron. Astrophys.* **641**, A6 (2020), [Erratum: *Astron. Astrophys.* 652, C4 (2021)], arXiv:1807.06209 [astro-ph.CO].
- [55] M. Monelli, E. Komatsu, A. E. Adler, M. Billi, P. Campeti, N. Dachlythra, A. J. Duivenvoorden, J. E. Gudmundsson, and M. Reinecke, Impact of half-wave plate systematics on the measurement of cosmic birefringence from CMB polarization, (2022), arXiv:2211.05685 [astro-ph.CO].
- [56] K. N. Abazajian, P. Adshead, Z. Ahmed, S. W. Allen, D. Alonso, K. S. Arnold, C. Baccigalupi, J. G. Bartlett, N. Battaglia, B. A. Benson, C. A. Bischoff, J. Borrill, V. Buza, E. Calabrese, R. Caldwell, J. E. Carlstrom, C. L. Chang, T. M. Crawford, F.-Y. Cyr-Racine, F. De Bernardis, T. de Haan, S. d. S. Alighieri, J. Dunkley, C. Dvorkin, J. Errard, G. Fabbian, S. Feeney, S. Ferraro, J. P. Filippini, R. Flauger, G. M. Fuller, V. Gluscevic, D. Green, D. Grin, E. Grohs, J. W. Henning, J. C. Hill, R. Hlozek, G. Holder, W. Holzapfel, W. Hu, K. M. Huffenberger, R. Keskitalo, L. Knox, A. Kosowsky, J. Kovac, E. D. Kovetz, C.-L. Kuo, A. Kusaka, M. L. Jeune, A. T. Lee, M. Lilley, M. Loverde, M. S. Madhavacheril, A. Mantz, D. J. E. Marsh, J. McMahon, P. D. Meerburg, J. Meyers, A. D. Miller, J. B. Munoz, H. N. Nguyen, M. D. Niemack, M. Peloso, J. Peloton, L. Pogosian, C. Pryke, M. Raveri, C. L. Reichardt, G. Rocha, A. Rotti, E. Schaan, M. M. Schmittfull, D. Scott, N. Sehgal, S. Shandera, B. D. Sherwin, T. L. Smith, L. Sorbo, G. D. Starkman, K. T. Story, A. van Engelen, J. D. Vieira, S. Watson, N. Whitehorn, and W. L. K. Wu, *Cmb-s4 science book*, first edition (2016).